**Investigation of Inter Rotor Spacing Effect on Aerodynamics and** 

Aeroacoustics of a Coaxial Rigid Rotor Helicopters in Full

**Configuration Using High-Fidelity Numerical Simulations** 

Sung U Kang, Seung Been Shin, Rho Shin Myong, Hakjin Lee a)

School of Aerospace Engineering, Gyeongsang National University, Jinju, Gyeongnam 52828, South Korea

<sup>a)</sup>Author to whom correspondence should be addressed: <u>hlee@gnu.ac.kr</u>

**Abstract** 

The coaxial rotor system, a key component of high-speed and long-range compound helicopters, eliminates

the need for a tail rotor. However, aerodynamic interactions between the upper and lower rotors can

substantially influence aerodynamic performance and noise generation. Inter-rotor spacing (IRS), defined as the

ratio of the vertical distance between the upper and lower rotors to the diameter is a critical design parameter

that affects rotor wake structure and blade-vortex interaction (BVI), particularly during forward flight. This

study investigates the effects of IRS and advance ratio on the unsteady aerodynamics and aeroacoustics of

coaxial rotors through high-fidelity numerical simulations. The simulations employ the Spalart-Allmaras

improved delayed detached eddy simulation model coupled with overset mesh techniques. Aeroacoustic analysis

is conducted using the Ffowcs Williams-Hawkings acoustic analogy. The full-configuration X2TD helicopter,

excluding the pusher propeller, serves as the baseline model. Results indicate that a greater IRS value leads to

higher thrust growth rates under low-speed forward flight conditions and reduces unsteady loading fluctuations.

Moreover, a greater IRS value mitigates BVI and loading noise, reducing the overall sound pressure levels.

Notably, acoustic differences between the isolated coaxial rotor and full-configuration models highlight the

influence of fuselage reflection, with downward noise propagation attenuated by up to 2 dB in the latter. These

findings provide valuable insights into IRS optimization for enhanced aerodynamic efficiency and noise

reduction in coaxial rotorcraft.

1

**Keywords**: Coaxial Rotor Helicopter, Inter-Rotor Spacing, Aerodynamics, Aeroacoustics, Computational Fluid Dynamics, SA-IDDES

# 1. Introduction

Conventional helicopters can perform vertical takeoff and landing (VTOL) and hover at low altitudes. However, their forward-flight speed, operational range, and payload capacity are lower compared to those of fixed-wing aircraft [1], preventing high-speed forward flight over long distances, which restricts their operational capabilities. Various VTOL rotorcrafts with different rotor configurations have been developed to overcome these limitations and enhance flight speed and range [2,3]. Bell designed the V-280 Valor, which utilizes tilt rotors to efficiently transition between helicopter and airplane modes [4], and Piasecki suggested the SpeedHawk X-49, which possesses a ducted fan at the rear of the fuselage to improve thrust efficiency [5]. Moreover, Eurocopter designed the X<sup>3</sup>, a compound helicopter with two tractor propellers mounted on the fuselage wings to enable high-speed forward flight [6]. Sikorsky-Boeing developed the SB>1 Defiant, which employs a coaxial rotor system as the main rotor to enhance lift performance and cruise speed [7-9]. Among various rotor systems, the coaxial rotor helicopter eliminates the need for a tail rotor, as its counter-rotating blades naturally counteract torque, improving stability and maneuverability [10]. Moreover, the coaxial rotor provides exceptional lift capacity and a compact design, making it highly suitable for operations in confined environments. Owing to these advantages, the coaxial rotor system is widely adopted in next-generation highspeed and long-range compound helicopters [11], urban air mobility platforms [12,13], unmanned aerial vehicles, and the Mars Helicopter. A coaxial rotor helicopter can achieve substantially higher aerodynamic efficiency than a conventional helicopter. Unlike a single-rotor helicopter, where lift is created on the advancing and retreating sides of the rotor blade, a lift-offset coaxial rotor primarily produces lift on the advancing side [14,15]. Hence, a coaxial rotor can generate ~1.7 times more thrust than a conventional helicopter within the same footprint, as the upper and lower rotors rotate in opposite directions to counteract torque [16]. Despite these advantages, the coaxial rotor system introduces complex aerodynamic interactions, particularly due to interaction between the counter-rotating rotors.

Rotor-wake interaction complicates the understanding of the aerodynamic and acoustic characteristics of coaxial rotor systems. Interaction between the upper and lower rotors in coaxial rotor systems creates complex flow interference, generating higher noise levels than conventional helicopters with a single main rotor [17]. One of the critical design parameters affecting these interference phenomena is inter-rotor spacing (IRS), defined as the ratio of the vertical distance between the upper and lower rotors to the rotor diameter. A smaller IRS value increases rotor-rotor interaction, leading to considerable vibrations and reduced maneuverability.

However, a greater IRS value results in a bulkier hub system, increasing drag and reducing aerodynamic efficiency during forward flight. Additionally, the forward-flight speed directly influences wake structure development, affecting interactional phenomena. Wake interference is particularly pronounced at low flight speed, where the unsteady wake flow originating from the upper rotor propagates into the lower rotor blades, primarily impacting noise generation and aerodynamic degradation [18]. Moreover, the presence of fuselage must be considered when analyzing the interactional aerodynamics and acoustics of a coaxial rotor system, as it substantially alters the flow environment compared to an isolated rotor configuration [19]. In a full configuration, the wakes generated by the upper and lower rotors can interact with one another and the fuselage, leading to complex flow interference effects. Furthermore, the wake shed from the fuselage may impinge on the lower surface of the rotor blade, modifying local inflow conditions and influencing aerodynamic loading and acoustic characteristics. Neglecting fuselage-induced interactions may result in an incomplete understanding of the performance of the rotor system under operating conditions. Therefore, a comprehensive understanding of the influences of IRS, forward-flight speed, and fuselage presence on the aerodynamic and acoustic characteristics of the coaxial rotor system is essential and has motivated several prior investigations.

Numerous studies have investigated the aerodynamic effects of IRS in coaxial rotor systems, particularly focusing on its influence on wake structure, thrust generation, and induced power under hover and forward-flight conditions. Leishman and Anathan [20] analyzed the influence of the upper rotor wake on the lower rotor in a coaxial rotor system under hover conditions at different IRS values using blade element momentum theory (BEMT), reporting that the wake generated by the upper rotor exhibited more considerable contraction as it approached the lower rotor with increasing IRS value. Ramasamy [21] conducted the experiment to explore the influence of IRS on the interference loss factor and wake instability under hover conditions. Nagashima and Nakanishi [22] investigated the impact of rotor—wake interference on wake structure and the performance of a coaxial rotor using the momentum equation and simplified free wake analysis. Qi et al. [23] predicted the thrust fluctuation of a coaxial rotor using Reynolds-Averaged Navier-Stokes (RANS) based on computational fluid dynamics (CFD) with overset mesh technique, demonstrating the overlap effect generated by the bound vortices of both rotors and the induction effect caused by wake interaction. Shinohara [24] experimentally measured the thrust and power variations of the upper and lower rotors in a coaxial rotor system under forward flight conditions at different advance ratios, reporting that the wake from the upper rotor was swept backward with increasing advance ratio. Kim and Brown [25] compared the power requirements of coaxial and conventional

rotors across different advance ratios under forward-flight conditions using vorticity transport model (VTM). They found that the coaxial rotor system exhibited different induced power requirements compared to the equivalent conventional rotor system. Park and Kwon [26] compared the aerodynamic performance and wake structure variations of an isolated coaxial rotor under hover and high-speed forward-flight conditions at different IRS values utilizing a RANS-based CFD and a computational grid based on an unstructured near-body region and a Cartesian off-body region. Hayami *et al.* [27] explored the effect of lift offset on the aerodynamic performance of an isolated coaxial rotor under forward-flight conditions using rFlow3D solver, developed at JAXA. The simulation results indicated that lift offset enhances the lift-to-drag ratio and minimizes thrust variations, although this effect decreases at high advance ratio. Jia and Lee [28, 29] analyzed both aerodynamic performance and acoustics of a lift-offset coaxial rotor in high-speed forward flight conditions using Spalart-Allmaras turbulence model with detached eddy simulation (SA-DES). They indicated that high speed forward flight conditions reduced the distribution of the sectional normal force than the isolated rotors. While numerous studies have explored the aerodynamic effects of IRS in coaxial rotor systems under hover and forward-flight conditions, most studies have primarily focused on an isolated rotor configuration with limited attention paid to fuselage interaction effects or unsteady flow mechanisms, which are critical to noise generation.

The aeroacoustic implications of IRS variations remain comparatively underexplored, particularly for full-configuration rotorcraft, including fuselage geometry. Sedlacek *et al.* [30] compared the acoustic characteristics of coaxial co-rotating and counter-rotating rotors under hover conditions to examine the rotation effect on noise level, indicating that the counter-rotating configuration produced significantly higher tonal noise due to 2 Nb/rev blade crossing interactions. Xu *et al.* [31] investigated the impact of IRS on the aeroacoustic characteristics of isolated coaxial counter-rotating propellers under hover conditions at different rotational speeds using RANS simulations and the Ffowcs Williams–Hawkings (FW–H) acoustic analogy. They found that a smaller IRS value increased the noise levels of the propellers, while varying the rotational speed reduced the peak sound pressure level by up to 3 dB. Qi *et al.* [32] analyzed the acoustic characteristics of an isolated coaxial rotor in forward-flight conditions under various advance ratio and lift offset conditions, revealing that an increased advance ratio shifted the rotor thickness noise toward the advancing side, while a higher lift offset intensified blade–vortex interaction (BVI) noise but reduced rotor-rotor interaction noise. Anusonti-Inthra [33] investigated the presence effects of the fuselage on aerodynamics and structural dynamics of coaxial rotor helicopter in forward flight using RANS-based CFD. Their results showed that the fuselage increased the higher harmonics components,

leading to affected the aerodynamic load and flap bending of the lower rotor. Kim et al. [34] analyzed the aerodynamics and acoustics characteristics of a coaxial rotor helicopter using VTM, and found that the acoustic signature of the helicopter is strongly affected by rotor-wake interaction phenomena. Kim et al. [35] investigated the aeroacoustic behavior of a coaxial rotor system under forward flight conditions, with a focus on rotor-fuselage interaction effects. The inclusion of fuselage increased thrust fluctuations and unsteady pressure loads, resulting in increase in the overall sound pressure levels by up to 2.5 dB. This study demonstrated that rotor-fuselage interaction notably alters the directivity and amplitude of loading and thickness noise components. Table 1 summarizes previous studies that investigated the aeroacoustic characteristics of the coaxial rotor system.

**Table 1.** Detailed review of aerodynamic and acoustic analyses of the coaxial rotor system.

Paper details	Research details	Fuselage	Numerical method
Xu et al. [31] (2020)	Investigating the impact of IRS on the aeroacoustic characteristics of isolated coaxial propellers under hover	X	RANS
Qi <i>et al.</i> [32] (2024)	Comparing the noise levels of isolated coaxial rotor under various advance ratio and lift offset conditions	X	RANS
Jia and Lee [28, 29] (2020, 2021)	Investigating aerodynamic performance and acoustics of a lift-offset isolated coaxial rotor	X	SA-DES
Kim <i>et al.</i> [35] (2019)	Exploring the rotor–fuselage interaction effects on aeroacoustics of coaxial rotor in forward-flight conditions	O	VLM
Anusonti-Inthra [33] (2019)	Numerical study of the effects of the presence of the fuselage on aerodynamic performance of coaxial rotorcraft	O	RANS
Kim <i>et al.</i> [34] (2009)	Investigating interactional aerodynamics and acoustics of coaxial rotor helicopter in forward flight	O	VTM
Present (2025)	Exploring IRS effects on aerodynamics and acoustics of coaxial rotor helicopter with fuselage interaction in low-and high-speed forward flight conditions	O	SA-IDDES

The main objective of this study was to investigate the influence of IRS on the interactional aerodynamics and acoustics of a full-configuration coaxial rotor helicopter under low- and high-speed forward-flight conditions. Two major gaps in the existing literature were identified. First, the aerodynamic and acoustic

interactions between the coaxial rotor system and the fuselage, as influenced by variations in IRS and forwardflight speed, remain unexplored. This research aimed to fill this gap in the literature by adopting a fullconfiguration model that includes the coaxial rotor and fuselage, enabling a more realistic assessment of the rotor-fuselage interaction effect on overall aerodynamic performance and noise level. Second, limited research has applied the DES model to analyze the unsteady aerodynamic forces and wake dynamics of the coaxial rotor system. Prior studies have relied on RANS-based approaches, which are inherently limited in capturing wake features critical to noise generation owing to their time-averaged nature. As accurate prediction of noise characteristics requires resolving these unsteady wake flow phenomena, this study employed the Spalart-Allmaras improved delayed DES (SA-IDDES) model, which enables improved representation of timedependent wake interactions and aerodynamic loading [36]. The use of DES and full-configuration modeling provided insights into the influence of coaxial rotor-fuselage interaction on thrust fluctuation, wake behavior, and noise radiation. Based on the results of the aerodynamic analysis, the Farassat 1A formulation with impermeable boundary conditions was utilized to evaluate the thickness and loading noise radiating from the full-configuration coaxial rotor helicopter. DES predictions of Harrington Rotor 1 and X2TD rotor models were compared against experimental results and available data for validation. Finally, the full-configuration X2TD coaxial rotor helicopter, excluding the pusher propeller, was employed to investigate interactional aerodynamics and acoustics under forward-flight conditions.

# 2. Computational Methods

### 2.1 Detached Eddy Simulation

This study employed the SA-IDDES model to analyze the aerodynamic and acoustic characteristics of the coaxial rotor helicopter. DES is a hybrid turbulence method that models the near-wall region using RANS to reduce computational costs, while large eddy simulation (LES) is applied in off-body regions to resolve coherent wake structures [37-39]. The wake structure behind the fuselage and rotor blades must be accurately captured considering its importance in analyzing the aerodynamic and acoustic characteristics of the coaxial rotor helicopter. Hence, the use of DES was essential in this study. While often utilized in rotorcraft simulations where periodic rotor wakes dominate the flow, unsteady RANS may not effectively capture transient wake structures and flow separation phenomena, particularly in cases involving complex wake interactions. As this study focused on the effects of IRS and advance ratio on rotor-rotor and rotor-fuselage interactions, DES was

employed to better resolve the wake structures and their influence on aerodynamic performance and noise characteristics. DES turbulence models solve the boundary layers and irrotational flow regions using a RANS-based approach. However, a sufficiently fine grid can emulate an LES subgrid-scale model in areas of detached flow, enabling the use of RANS in boundary layers and LES in unsteady separated regions, exploiting the advantages of both techniques. Turbulence models in RANS can be divided into Spalart–Allmaras DES, elliptic blending k– $\epsilon$  DES, and shear stress transport k– $\omega$  DES models. This study employed the Spalart–Allmaras turbulence model owing to its ability to analyze large and complex flow fields with low computational cost and high accuracy during the turbulence analysis of near-wall surfaces [40]. The mean velocity ( $\bar{\nu}$ ) from RANS and filtered velocity ( $\bar{\nu}$ ) from LES can be expressed by the momentum equations Eqs. (1) and (2), respectively:

$$\frac{\partial}{\partial t}(\rho \overline{\mathbf{v}}) + \nabla \cdot (\rho \overline{\mathbf{v}} \otimes \overline{\mathbf{v}}) = -\nabla \cdot \overline{\mathbf{p}} \mathbf{I} + \nabla \cdot (\overline{\mathbf{T}} + \mathbf{T}_{RANS}) + \mathbf{f}_{\mathbf{b}}, \tag{1}$$

$$\frac{\partial}{\partial t}(\rho \tilde{\mathbf{v}}) + \nabla \cdot (\rho \tilde{\mathbf{v}} \otimes \tilde{\mathbf{v}}) = -\nabla \cdot \tilde{\mathbf{p}} \mathbf{I} + \nabla \cdot (\tilde{\mathbf{T}} + \mathbf{T}_{SGS}) + \mathbf{f}_{\mathbf{b}}, \tag{2}$$

where  $\rho$  is the density, p is the pressure,  $f_h$  is the resultant of body forces, and T is the stress tensor.

The Reynolds stress tensor  $(T_{RANS})$  is defined as a function of time and length scale, as expressed in Eq. (3):

$$\mathbf{T}_{RANS} = f(\nabla \cdot \overline{\mathbf{v}}, \mathbf{k}, \varepsilon) , \qquad (3)$$

where k is to the turbulent kinetic energy and  $\varepsilon$  is to the turbulent dissipation rate. For LES, the sub-grid scale stress (T<sub>SGS</sub>) is calculated with  $\widetilde{v}$  and the local measure of the grid size ( $\Delta$ ), as expressed in Eq. (4):

$$\mathbf{T}_{SGS} = f(\nabla \cdot \tilde{\mathbf{v}}, \Delta), \tag{4}$$

In Eq. (4), the widths of the filter and length scale are the most important factors. These are adopted in the definition of subgrid-scale eddy viscosity but also in many models for the transition region. The similarities between Eqs. (1) and (2) allow for a unified approach in solving for quantity, as represented in Eq. (5):

$$\frac{\partial}{\partial t}(\rho \hat{\mathbf{v}}) + \nabla \cdot (\rho \hat{\mathbf{v}} \otimes \hat{\mathbf{v}}) = -\nabla \cdot \hat{\mathbf{p}} \mathbf{I} + \nabla \cdot (\hat{\mathbf{T}} + \mathbf{T}_{RANS}) + \mathbf{f_b},$$
(5)

where  $\hat{\mathbf{v}}$  is to the predicted velocity and I is to the identity tensor.

The turbulent length scale, defined as a measure of the extent to which turbulent energy influences different regions of the flow domain, is important when modeling the energy transfer process from larger to smaller vortices. The damping function ( $f\Delta$ ) is adopted in turbulence models to regulate the turbulent viscosity

distribution. By reducing the turbulent viscosity in regions with low turbulence intensity, such as in near-wall regions, the damping function improves the accuracy of capturing real physical phenomena. Turbulence model  $(T_{model})$  is expressed in Eq. (6) as follows:

$$\mathbf{T}_{model} = f\Delta(\frac{\Delta}{l_k})\mathbf{T}_{RANS} \tag{6}$$

where l<sub>k</sub> is the turbulent length scale.

This study implemented the SA-IDDES model using blending functions  $f_B$  and  $f_e$  to achieve wall-modeled LES), as expressed by Eqs. (7) and (8), respectively [41]:

$$f_B = \min[2\exp(-9\alpha^2), 1] \tag{7}$$

$$f_e = \max[(f_{e1} - 1), 0] \psi f_{e2}$$
 (8)

where  $\alpha$  represents a parameter that defines a specific distance ratio within the SA-IDDES model. The functions  $f_{e1}$  and  $f_{e2}$  vary depending on whether the value of  $\alpha$  is higher or lower than zero, while  $\psi$  is a function that accounts for turbulence correction in flows with a low Reynolds number.

The unsteady implicit method was utilized in unsteady simulations, and time integration was accomplished using the dual time stepping technique, with 15 sub-iterations per time step and a time step of 1° per rotor blade rotation angle to improve computational efficiency. The study employed Roe's flux difference splitting scheme for the inviscid convective terms. The 3rd order MUSCL scheme was employed for spatial discretization using the central differencing method, which calculates variable gradients using the averaged values of adjacent grid points. The Venkatakrishnan limiter was adopted to control numerical oscillations.

### 2.2 Ffowcs Williams-Hawkings Acoustic Analogy

Among various noise sources in rotorcraft, rotor noise, generated by unsteady, three-dimensional aerodynamic phenomena, is one of the most important contributors to the overall acoustic signature. Rotor noise is categorized based on several generation mechanism, with each associated with different sources and flow interactions around rotor blades. Thickness noise arises from the displacement of air caused by rotor blade geometry, leading to acoustic pressure fluctuations due to local fluid compression and expansion. Loading noise is generated by aerodynamic forces acting on the rotor blade surface. BVI noise occurs when a rotating blade encounters strong tip vortices shed from the preceding rotor blades, producing impulsive acoustic events. High-

speed impulsive noise is emitted from the advancing side of the rotor blade at high tip Mach numbers, which typically occurs during high-speed forward flight [42]. In the coaxial rotor configuration, interactional noise is generated because of aerodynamic interference between upper and lower rotors. Mutual interaction of their wake systems induces substantial variations in the local flow field, imposing unsteady aerodynamic loading on both rotors. This interaction leads to time-varying blade forces that modify aerodynamic performance and serve as a key source of fluctuating loading noise. Such wake-induced interactions are particularly sensitive to parameters such as IRS and advance ratio, making them essential considerations in the aeroacoustic analysis of the coaxial rotor system.

Herein, the Farassat 1A formulation, which is derived from the theoretical solution to the FW–H equation, is employed to predict the noise generated by the full-configuration coaxial rotor helicopter [43]. The acoustic analogy is applied under impermeable boundary conditions to evaluate thickness and loading noise generated by the fuselage and rotor blade surfaces. Eq. (9) presents the Farassat 1A formulation, in which the total acoustic pressure is expressed as the sum of the contributions from thickness noise (p'<sub>T</sub>) and loading noise (p'<sub>L</sub>) sources [44]:

$$p'(\mathbf{x},t) = p'_{T}(\mathbf{x},t) + p'_{L}(\mathbf{x},t) , \qquad (9)$$

where x is the position of the observer and t is the observer time.

Eqs. (10) and (11) represent the acoustic pressure of thickness and loading noise, respectively:

$$p'_{T}(\mathbf{x},t) = \frac{1}{4\pi} \int_{f=0} \left[ \frac{\rho_{0}(\dot{v}_{n} + v_{\dot{n}})}{r |1 - M_{r}|^{2}} \right]_{ret} dS + \frac{1}{4\pi} \int_{f=0} \left[ \frac{\rho_{0}v_{n}(r\dot{M}_{r} + a_{0}M_{r} - a_{0}M^{2})}{r^{2} |1 - M_{r}|^{3}} \right]_{ret} dS$$

$$p'_{L}(\mathbf{x},t) = \frac{1}{4\pi a_{0}} \int_{f=0} \left[ \frac{\dot{l}_{r}}{r |1 - M_{r}|^{2}} \right]_{ret} dS + \frac{1}{4\pi} \int_{f=0} \left[ \frac{l_{r} - l_{M}}{r^{2} |1 - M_{r}|^{2}} \right]_{ret} dS$$

$$+ \frac{1}{4\pi a_{0}} \int_{f=0} \left[ \frac{l_{r} \left( r\dot{M}_{r} + a_{0}M_{r} - a_{0}M^{2} \right)}{r^{2} |1 - M_{r}|^{3}} \right]_{ret} dS$$

$$+ \frac{1}{4\pi a_{0}} \int_{f=0} \left[ \frac{l_{r} \left( r\dot{M}_{r} + a_{0}M_{r} - a_{0}M^{2} \right)}{r^{2} |1 - M_{r}|^{3}} \right]_{ret} dS$$

$$+ \frac{1}{4\pi a_{0}} \int_{f=0} \left[ \frac{l_{r} \left( r\dot{M}_{r} + a_{0}M_{r} - a_{0}M^{2} \right)}{r^{2} |1 - M_{r}|^{3}} \right]_{ret} dS$$

$$+ \frac{1}{4\pi a_{0}} \int_{f=0} \left[ \frac{l_{r} \left( r\dot{M}_{r} + a_{0}M_{r} - a_{0}M^{2} \right)}{r^{2} |1 - M_{r}|^{3}} \right]_{ret} dS$$

$$+ \frac{1}{4\pi a_{0}} \int_{f=0} \left[ \frac{l_{r} \left( r\dot{M}_{r} + a_{0}M_{r} - a_{0}M^{2} \right)}{r^{2} |1 - M_{r}|^{3}} \right]_{ret} dS$$

$$+ \frac{1}{4\pi a_{0}} \int_{f=0} \left[ \frac{l_{r} \left( r\dot{M}_{r} + a_{0}M_{r} - a_{0}M^{2} \right)}{r^{2} |1 - M_{r}|^{3}} \right]_{ret} dS$$

$$+ \frac{1}{4\pi a_{0}} \int_{f=0} \left[ \frac{l_{r} \left( r\dot{M}_{r} + a_{0}M_{r} - a_{0}M^{2} \right)}{r^{2} |1 - M_{r}|^{3}} \right]_{ret} dS$$

$$+ \frac{1}{4\pi a_{0}} \int_{f=0} \left[ \frac{l_{r} \left( r\dot{M}_{r} + a_{0}M_{r} - a_{0}M^{2} \right)}{r^{2} |1 - M_{r}|^{3}} \right]_{ret} dS$$

where  $v_n$  represents the vertical velocity at the surface,  $\alpha_0$  is the acoustic speed,  $M_r$  is the Mach number along the direction from the noise source to the receiver, and  $l_r$  refers to the load vector on the rotor blade. A spatial delay is equal to the time (t) required for the sound wave to move through the spatial distance (r) between the noise source (x) and the observer (y). The values in brackets are calculated at the retarded time ( $\tau$ ) [45], as expressed in Eq. (12):

$$\tau = t - \frac{|\mathbf{x} - \mathbf{y}|}{a_0} \tag{12}$$

#### 2.3 Computational Validation

The accuracy of numerical methods must be validated to accurately predict the aerodynamics and acoustics of a coaxial rotor under forward-flight conditions through computational analysis. In particular, given that the aerodynamic forces on the rotor blades substantially influence loading noise, precise aerodynamic predictions are crucial for improving the accuracy of noise analysis. To verify the validity of the numerical methods employed in this study, the thrust and power of an isolated coaxial rotor at different advance ratios were analyzed and compared with experimental data. The specific planform of the adopted Harrington Rotor 1, designed by NASA for experimental purposes, is shown in Fig. 1 [46]. The Harrington Rotor 1 model comprises six different airfoil sections, has a taper ratio of 0.39, and does not include sweepback or twist angles. The power required to produce the same thrust at different advance ratios was measured. Trim values from a previous study were adopted to determine the corresponding collective and cyclic pitch angles, as summarized in Table 2 [47]. The relative velocity difference between the advancing and retreating sides of the upper and lower rotor blades became more significant with increasing advance ratio. For coaxial counter-rotating rotors operating at the same rotational speed but at different advance ratios, faster forward flight required an increased shaft tilt angle and higher pressure on the upper surface of the rotor blades. To generate the same thrust under these conditions, the collective pitch angle was increased, while the longitudinal cyclic pitch angle was also increased to reduce the thrust difference between the advancing and retreating sides of the rotor blades. Conversely, the lateral cyclic pitch angle was decreased to minimize the moment at azimuth angles of 0° and 180°, where the relative velocity difference was minimal.

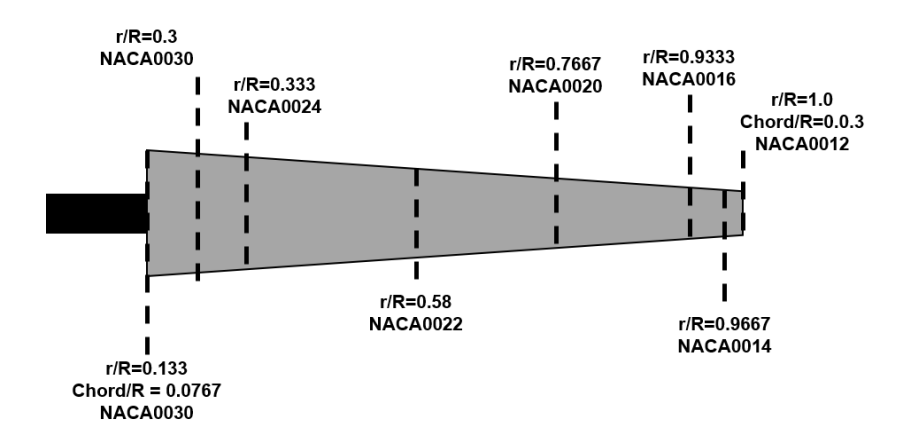


Fig. 1. Rotor blade planform for Harrington Rotor 1.

**Table 2.** Trim solutions of Harrington Rotor 1 at different advance ratios.

Advance ratio (μ)	Upper rotor			Lower rotor		
Advance rano (µ)	$\Theta_0$	$\theta_{1s}$	$\theta_{1c}$	$\Theta_0$	$\theta_{\rm 1s}$	$\theta_{1c}$
0.12	8.07°	-2.75°	1.05°	7.98°	-2.43°	1.32°
0.24	10.68°	-5.9°	0.36°	10.65°	-5.75°	0.5°

The thrust and power analysis results for the Harrington Rotor 1 at different advance ratios are presented in Fig. 2. Constant thrust was maintained regardless of advance ratio, and the analysis was performed using the SA-IDDES model. The predicted thrust and power exhibited error ranges of 1.36%–4.34% and 0.32%–3.66% compared to the experimental values, respectively. In particular, the predicted power exhibited high accuracy at an advance ratio of 0.12, with only 0.3% deviation from the experimental data. The relative velocity difference between the advancing and retreating sides of the rotor blade increased with increasing advance ratio, leading to thrust imbalance. The blade pitch angle was reduced on the advancing side and increased on the retreating side to counteract this effect, ensuring thrust balance. Consequently, the higher advance ratio resulted in more significant thrust variations at the azimuth angle. However, the thrust variation was minimal at the lower advance ratio of 0.12, leading to predicted results that closely matched the experimental data.

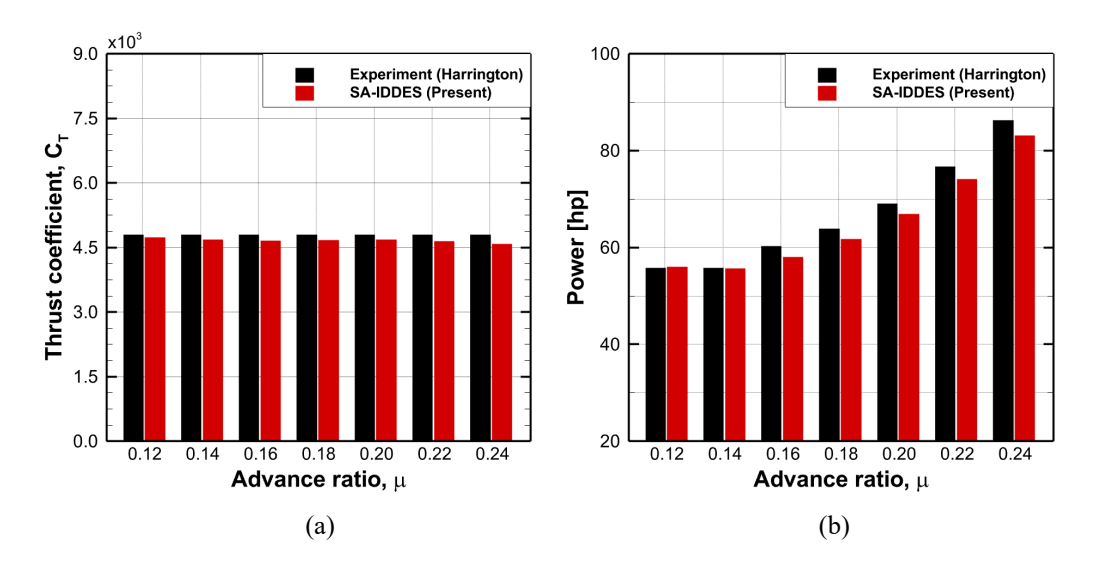
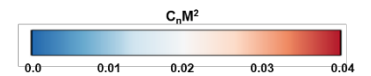


Fig. 2. Comparison of thrust and power of Harrington Rotor 1 as a function of advance ratio: (a) thrust coefficient  $(C_T)$ ; (b) required power.

To further assess the validity of the SA-IDDES model in capturing unsteady wake structures in a coaxial rotor system, the predicted wake skew angles of the Harrington rotor 1 were compared with previously reported high-fidelity computational results under forward flight conditions. At advance ratios of  $\mu = 0.12$  and  $\mu = 0.24$ , the SA-IDDES simulations predicted approximately wake skew angles of 80° and 89°, respectively, which closely match the reference values reported in the literature [47]. These results demonstrate that the SA-IDDES model can accurately capture the evolution characteristics of the rotor wake under forward flight. Moreover, to assess the predictive fidelity of the SA-IDDES model in resolving unsteady aerodynamic phenomena in coaxial rotor systems, a detailed comparative analysis was performed against the RANS model using the Harrington rotor 1 configuration at an advance ratio of  $\mu = 0.12$ . While the RANS model exhibited a deviation of 6.25% from the experimental thrust value, the SA-IDDES model showed a significantly lower error of 1.36%. To identify the source of this discrepancy, Figs. 3 and 4 compare the azimuthal distributions of the normal force and its temporal derivative over the lower rotor blade. While both simulations adopted identical geometric and boundary conditions, the two methods exhibited marked differences in capturing the spatial and temporal characteristics of rotor-wake interactions. As shown in Fig. 3, the azimuthal distribution of the normal force coefficient (C<sub>n</sub>M<sup>2</sup>) on the lower rotor blade reveals that the SA-IDDES method captures higher and more spatially varied loading near  $\psi \approx 90^{\circ}$  compared to RANS. This region corresponds to the location where the advancing blade of the lower rotor encounters the retreating wake of the upper rotor, thereby inducing strong inter-rotor interference. Fig. 4 further highlights this difference by illustrating the time derivative of the normal force coefficient (d C<sub>n</sub>M<sup>2</sup>/d t). The SA-IDDES solution clearly captures sharper temporal variations and more pronounced loading fluctuations in the outer blade region, especially near  $\psi \approx 90^{\circ}$ , indicative of BVI events. In contrast, the RANS method yields underestimated load variations, failing to reflect the transient nature of the aerodynamic loads. These results clearly demonstrate that the SA-IDDES model offers superior resolution of interactional aerodynamic effects in coaxial rotor systems, including the accurate prediction of unsteady flow features, such as BVI. The improved fidelity in capturing these phenomena is essential not only for reliable aerodynamic analysis but also for accurate acoustic prediction.



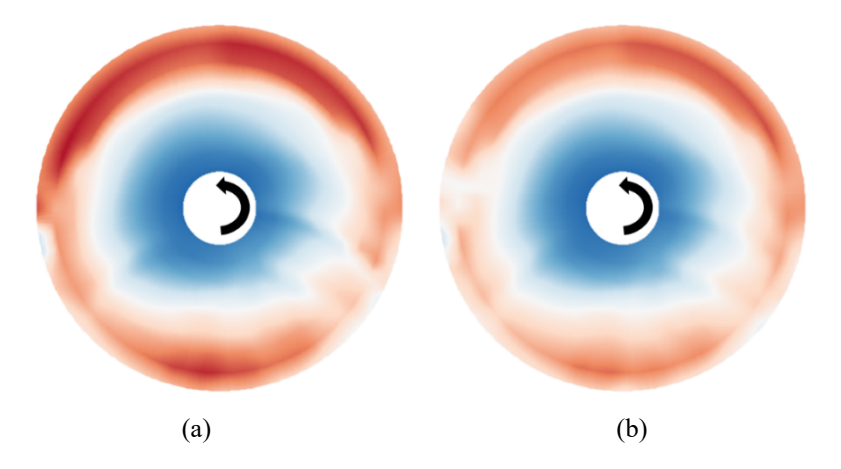
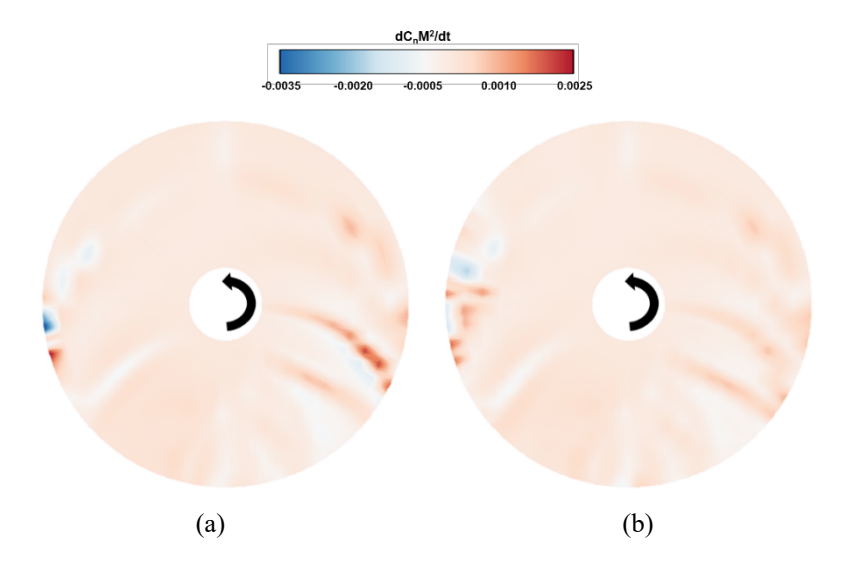


Fig. 3. Comparison of azimuthal distribution of normal force coefficient ( $C_nM^2$ ) on the lower rotor blade of Harrington rotor 1 at an advance ratio of  $\mu = 0.12$ : (a) SA-IDDES; (b) RANS.



**Fig. 4.** Comparison of time derivative of the normal force coefficient ( $d \, C_n M^2 / d \, t$ ) on the lower rotor blade of Harrington rotor 1 at  $\mu = 0.12$ : (a) SA-IDDES; (b) RANS.

# 3. Computational Setup

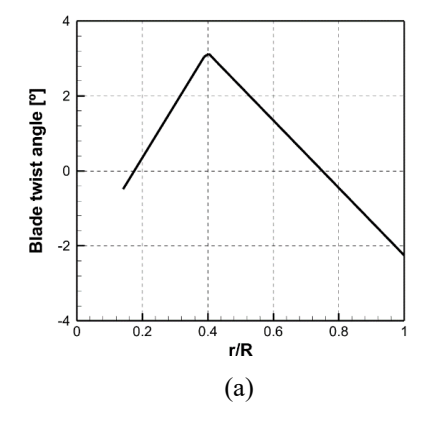
# 3.1 X2TD Helicopter Model

In this study, the Sikorsky X2TD helicopter was employed to explore the interactional aerodynamics and acoustics of a coaxial rotor under forward-flight conditions at varying IRS values and advance ratios. The geometric information of the X2TD helicopter model is listed in Table 3 [48]. A coaxial rotor system with the fuselage was modeled, excluding the pusher propeller. The upper and lower rotors rotated counter-clockwise

and clockwise, respectively, and each rotor had four blades with a radius of 4.023 m. The twist angle and thickness distribution of the rotor blades along the radial direction are shown in Fig. 5 [49]. To define the sectional geometry of the X2TD main rotor blade, representative airfoil profiles were extracted at key spanwise locations based on publicly available data. The original X2TD rotor design employs a combination of elliptic airfoils in the inboard region to mitigate drag penalties associated with reverse flow phenomena encountered during high-speed forward flight. Moreover, a transonic airfoil is adopted toward the outboard region to minimize compressibility effects, transitioning from a high-lift, sharp trailing-edge airfoil at the mid-span. In this study, airfoil sections were selected to closely approximate the blade geometry of the X2TD configuration, under the assumption that the upper and lower rotors share identical planforms. The DBLN-5262 elliptical airfoil was implemented in the spanwise region from 0.142R to 0.331R (where R denotes the rotor radius). The SC1012-R8 airfoil was applied from 0.468R to 0.568R to represent the mid-span section, while the SSCA-09 transonic airfoil was employed from 0.6R to the blade tip. Detailed information on the selected airfoils and their spanwise distribution is provided in Table 4.

Table 3. Model properties of X2TD configuration.

Properties	Specification
Gross Weight [kg]	2700
Radius, R [m]	4.023
Number of Rotors,	2
Blades per Rotor, N <sub>b</sub>	4
Total Solidity, $\sigma_{TW}$	0.14
Blade Aspect Ratio	19.2
Rotor Vertical Separation [m]	0.443
Fuselage Length [m]	9.1



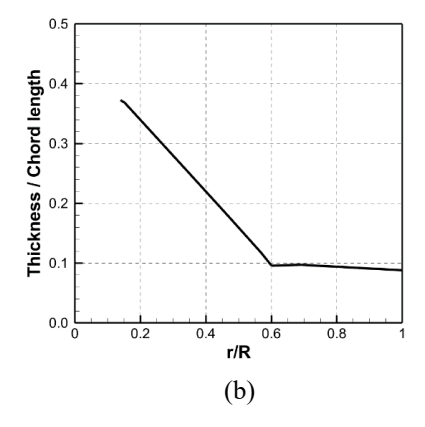


**Fig. 5.** Planform geometry of X2TD rotor blade: (a) blade twist angle distribution; (b) thickness distribution.

**Table 4.** Airfoil cross-sections of X2TD rotor blade [47].

Radial location (r/R)	Airfoil profile
0.142	DBLN-526
0.331	DBLN-526
0.468	SC1012-R8
0.568	SC1012-R8
0.600	SSCA-09
1.000	SSCA-09

#### 3.2 Computational Mesh and Convergence Test

The computational domain and grid system employed in the SA-IDDES model are depicted in Fig. 6. The domain size was set to 10D × 10D × 20D (where D denotes the rotor diameter) in the spanwise (W), vertical (H), and streamwise (L) directions, respectively. This domain extent was selected to ensure minimal boundary interference and allow sufficient wake structure development, particularly under forward-flight conditions. No-slip boundary conditions were imposed on all solid surfaces, while a velocity inlet and pressure outlet were applied at the upstream and far-field boundaries, respectively. Rotor blade pitching motion was incorporated using an overset mesh technique to enable accurate treatment of blade kinematics and rotor–wake interaction without grid distortion. Approximately 76 million cells were employed in the full-configuration model, which included the coaxial rotor system and fuselage. The grid topology consisted of a fine near-body mesh to resolve the boundary layers and rotor wake structures and a coarser background mesh for the far-field region (Fig. 7). The grid resolution near the rotor blade surface was refined to capture tip vortex roll-up and unsteady BVI phenomena. The selected mesh configuration for the full-configuration model was determined based on a detailed grid sensitivity analysis using the isolated coaxial rotor model. The final mesh size ensures grid-converged solutions in terms of both aerodynamic loads and acoustic predictions while maintaining computational efficiency.

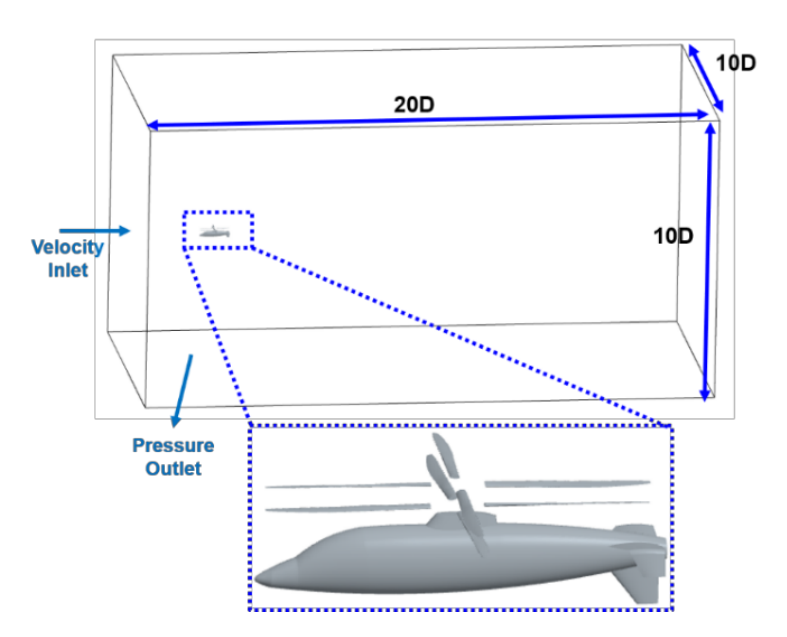
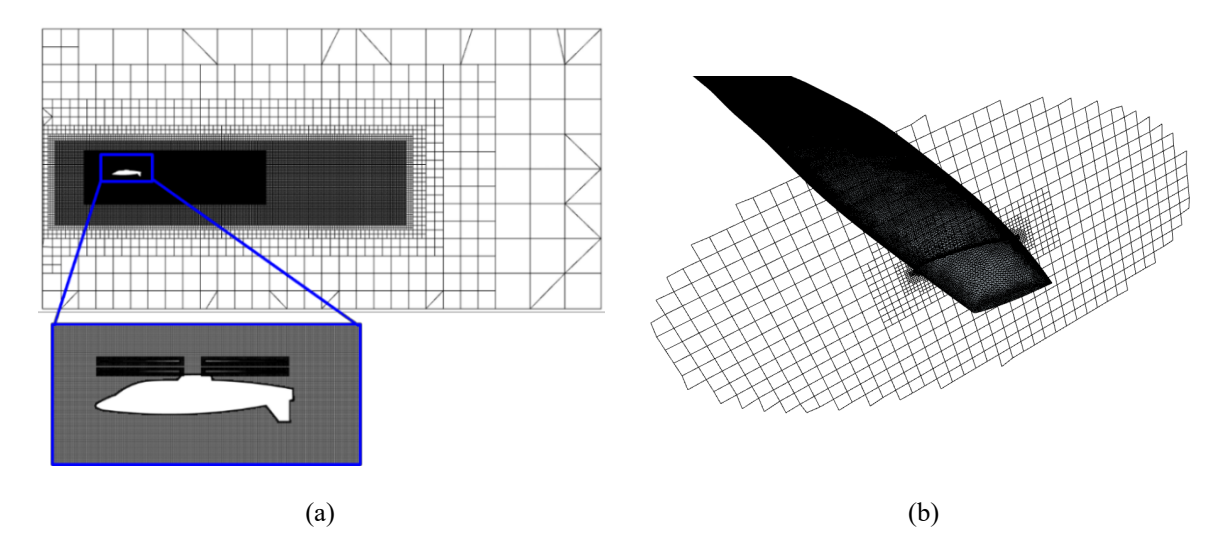


Fig. 5. Computational domain for full-configuration X2TD helicopter.



**Fig. 7.** Computational grid system for X2TD configuration: (a) off-body grid system; (b) near-body grid system.

As mentioned above, a grid resolution sensitivity analysis was conducted to determine the appropriate mesh density for accurate aerodynamic prediction while maintaining reasonable computational cost. Table 5 presents the time-averaged thrust over one rotor revolution for the isolated coaxial rotor model under low-speed forwardflight conditions depending on the mesh resolution (i.e., total cell count), and wall-clock simulation time. Four different mesh resolutions were evaluated, with total grid sizes ranging from 44 million to 74 million computational cells. The computational simulations were performed using parallel computing on a highperformance computing cluster equipped with Intel® Xeon® Gold 6230R CPUs operating at 2.1 GHz. In total, 512 physical cores were utilized for the numerical analysis. A monotonic increase in thrust prediction was observed with increasing mesh refinement. Specifically, the 60 million cell mesh yielded a thrust gain of approximately 2.0% compared to the 54 million cell mesh. Further increasing the grid size to 74 million cells resulted in an additional thrust gain of only 0.4% while incurring a notable increase in computational cost—approximately an additional 6 h. Considering the trade-off between computational efficiency and predictive accuracy, the 60 million cell mesh was selected as the baseline for subsequent analyses. Under these conditions, the simulation of six rotor revolutions for the isolated coaxial rotor model required approximately 28 h. In this configuration, the minimum grid spacing near the rotor surface was set to 2 mm, corresponding to approximately 0.75% of the local chord length at 75% span. The surface mesh was refined locally along critical regions of the rotor blade, including the leading and trailing edges, blade root, and blade tip. Particular attention was given to the blade tip region where strong pressure gradients and boundary layer development were expected. To accurately resolve the near-wall viscous sublayer, the height of the first cell adjacent to the wall

was set to maintain a non-dimensional wall distance ( $y^+$ ) of <1 at the blade tip leading edge. Under these conditions, the first cell height was approximately 0.003 mm. The boundary layer mesh was structured with 20 prism layers using a growth rate of 1.1, yielding a total boundary layer thickness of approximately 0.016 mm to ensure adequate resolution of wall-bounded flow features while preserving mesh quality. The remainder of the computational domain was discretized using unstructured polyhedral and hexahedral elements, adopting progressive coarsening toward the far field.

**Table 5.** Mesh convergence test results of isolated coaxial rotor at  $\mu = 0.15$ 

Total mesh (million cells)	Computational time (h)	Averaged thrust (N)
44	18	26,900
54	26	27,100
60	30	27,500
74	36	27,600

To verify the adequacy of the selected mesh resolution prior to analyzing the effects of IRS and advance ratio in the full-configuration model, the aerodynamic performance of the isolated coaxial rotor model was compared with results from previously published high-fidelity computational studies [47, 49]. This validation step ensured that the computational setup was capable of accurately capturing the unsteady aerodynamic behavior of the coaxial rotors across a range of forward-flight conditions. Figs. 8 and 9 present comparisons of the sectional normal force coefficient as a function of azimuth angle at representative radial positions (r/R = 0.30 and 0.85) and advance ratios ( $\mu = 0.15$  and 0.41). At  $\mu = 0.15$ , the numerical solution accurately captured the peak near the  $15^{\circ}$  azimuth and gradual increase in loading beyond  $270^{\circ}$  at r/R = 0.30, as well as the sharp unloading and periodic fluctuation near the 135° azimuth at r/R = 0.85—features associated with rotor-rotor interaction and BVI. At  $\mu = 0.41$ , more pronounced unsteadiness was observed in the loading distribution at r/R = 0.30, while the sharp rise in normal force near  $360^{\circ}$  at r/R = 0.85 was also well predicted. The close agreement with previously reported results confirmed the validity of the simulation framework in capturing the essential aerodynamic features of the X2TD coaxial rotor system under forward-flight conditions. Moreover, the numerical results for the isolated coaxial rotor model demonstrated excellent agreement with the high-fidelity reference data, confirming that the selected mesh resolution and simulation framework were capable of accurately resolving unsteady aerodynamic phenomena under forward-flight conditions

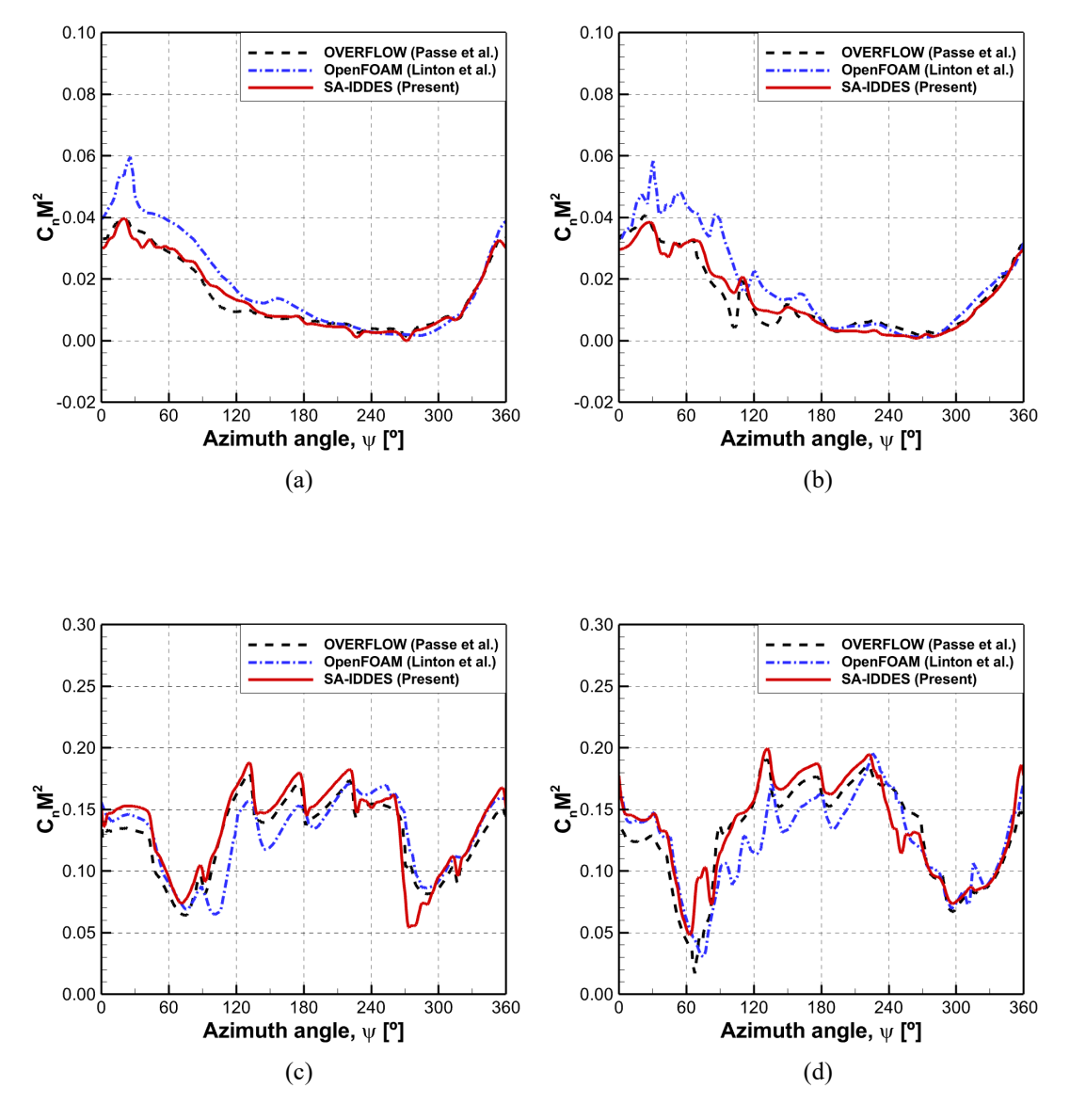


Fig. 8. Comparison of sectional normal force  $(C_nM^2)$  as a function of azimuth angle at  $\mu=0.15$ : (a) upper rotor at r/R=0.30; (b) lower rotor at r/R=0.30; (c) upper rotor at r/R=0.85; (d) lower rotor at r/R=0.85.

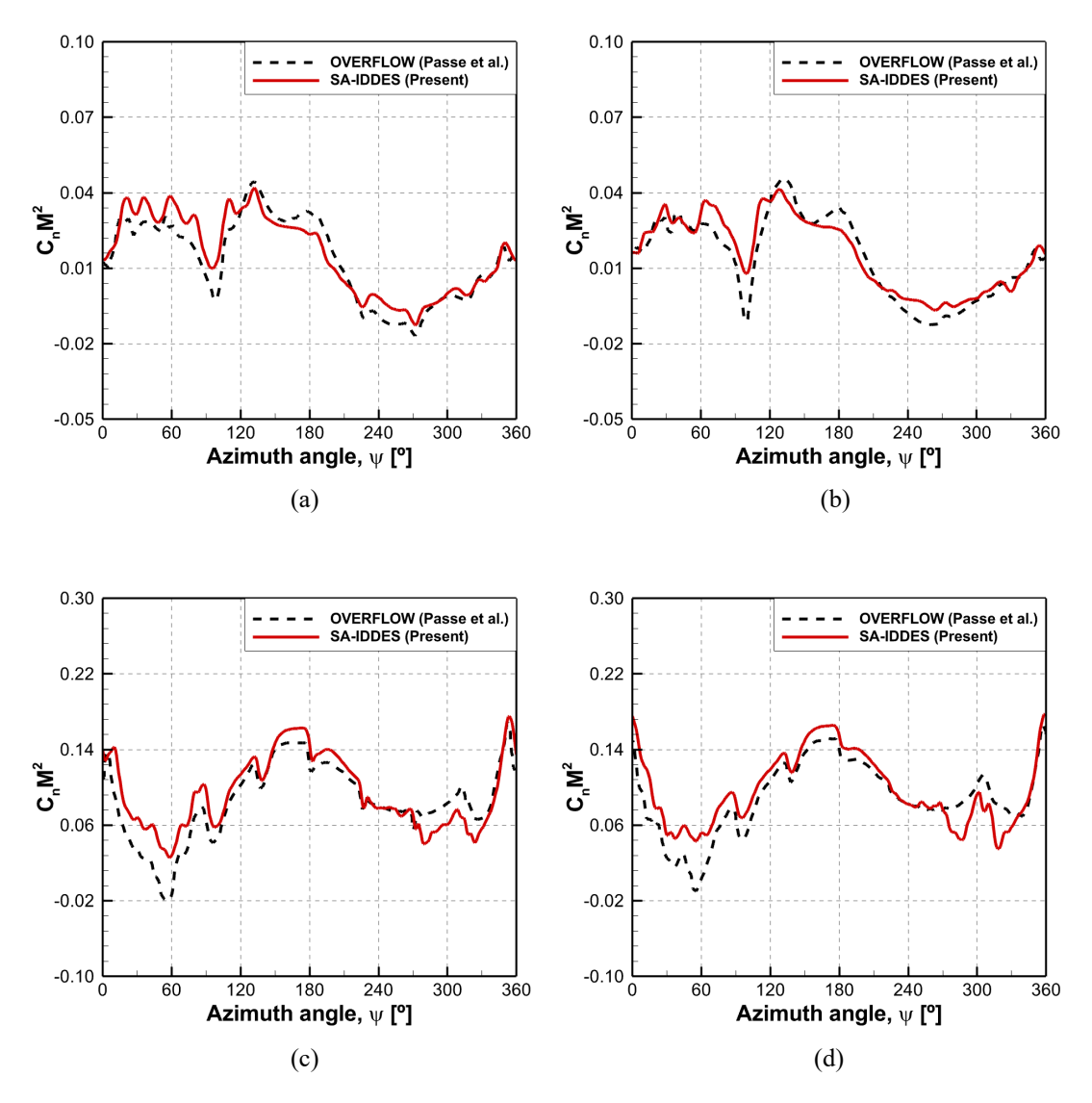


Fig. 9. Comparison of sectional normal force  $(C_nM^2)$  as a function of azimuth angle  $\mu = 0.41$ : (a) upper rotor at r/R = 0.30; (b) lower rotor at r/R = 0.30; (c) upper rotor at r/R = 0.85; (d) lower rotor at r/R = 0.85.

## 3.3 Simulation Conditions

The simulation conditions for forward-flight analysis of the X2TD helicopter are summarized in Table 6. All computations were conducted assuming standard atmospheric conditions at an altitude of 4000 ft. The rotor blade operated at a constant rotational speed of 446 RPM, corresponding to a blade tip Mach number of approximately 0.556. The IRS value was set to 0.443 m, corresponding to 0.055D. To investigate the influence of IRS on the aerodynamic and aeroacoustic characteristics of the X2TD helicopter, three IRS values were considered: baseline (original spacing) and 1.5 and 2.0 times the baseline spacing. Advance ratios of  $\mu = 0.15$ 

and  $\mu=0.41$  were adopted to represent low- and high-speed forward-flight conditions, respectively. Each simulation was performed over six rotor revolutions to ensure sufficient temporal resolution for frequency domain acoustic analysis. The aerodynamic solution reached a periodic steady state after two rotor revolutions, beyond which the data were extracted for analysis.

Table 6. Flight simulation conditions.

Properties	Specification
IRS (H/D)	0.055, 0.083, 0.11
Advance Ratio	0.15, 0.41
Reynolds Number	$2.5  imes 10^6$
Rotation Speed	446 RPM
Tip Mach Number	0.556
Flight Altitude	4000 ft
Pressure	87,494 Pa

During forward flight, the relative inflow velocity experienced by rotor blades varies continuously with azimuth angle due to the superposition of rotational and translational motions. Rotor blades encounter the highest relative velocities on the advancing side, which can lead to transonic flow conditions and shock wave formation at high tip Mach numbers. By contrast, rotor blades on the retreating side experience much lower relative velocities, increasing the risk of flow separation and dynamic stall. These effects result in an asymmetric aerodynamic load distribution across the rotor disk, which becomes even more complex in the coaxial rotor system due to aerodynamic interference between the upper and lower rotors. Notably, the advancing and retreating rotor blades occupy the same azimuthal positions but rotate in opposite directions, leading to intricate mutual wake interactions and unsteady rotor blade loading. To satisfy the force and moment balance requirements of the rotor system and minimize lift imbalance, periodic variation in rotor blade pitch—typically through cyclic pitch control—is essential.

Herein, trim analysis was performed by prescribing azimuth-dependent pitch angles for the upper and lower rotor blades, as expressed in Eqs. (13) and (14):

$$\theta_U = \theta_{0,U} + \theta_{1c,U} \cos(\psi) + \theta_{1s,U} \sin(\psi)$$
(13)

$$\theta_L = \theta_{0,L} + \theta_{1c,L} \cos(\psi) + \theta_{1s,L} \sin(\psi)$$
(14)

where  $\theta_U$  and  $\theta_L$  denote the blade pitch angles of the upper and lower rotors, respectively, expressed as harmonic functions of the azimuth angle ( $\psi$ ). Specifically,  $\theta_{0,U}$  and  $\theta_{0,L}$  represent the collective pitch angles for the upper and lower rotors, respectively, which primarily control the thrust magnitude, while  $\theta_{1c,U}$ ,  $\theta_{1c,L}$ ,  $\theta_{1s,U}$ , and  $\theta_{1s,L}$ , refer to the cyclic pitch angles, which govern the longitudinal and lateral responses, thereby generating the required rolling and pitching moments to balance the rotorcraft during forward flight. These pitch profiles were adjusted to satisfy force and moment equilibrium under each flight condition considered.

In this study, the numerical trim procedure was not integrated into the present simulation framework. Instead of solving for the trimmed state through an iterative process, the collective and cyclic pitch angles were prescribed based on previously validated reference data, ensuring that the rotorcraft was analyzed under a physically representative trimmed condition. While this approach restricts the general applicability of the numerical simulation to various rotor configurations and flight conditions, the primary objective was to investigate the aerodynamic and acoustic characteristics arising from the interaction between the coaxial rotor system and the fuselage under a known trimmed flight condition. Thus, despite the absence of a trim module, the present results remain meaningful for understanding the fundamental aerodynamic and acoustic effects associated with inter-rotor spacing in a full-configuration coaxial rotor helicopter.

This study employed collective and cyclic pitch angles obtained from published reference data [47]. The target thrust and pitching moment for each advance ratio were defined as follows: at  $\mu=0.15$ , the rotor system was trimmed to generate a thrust of 25,700 N and pitching moment of 6800 Nm, while at  $\mu=0.41$ , the corresponding targets were 22,300 N and 3600 Nm. The corresponding blade pitch inputs, comprising collective and cyclic components, used to achieve these conditions are summarized in Table 7. To satisfy the trim requirements, the rotor shaft tilt angles were prescribed as fixed inputs for each case. Shaft tilt angles of  $-0.44^{\circ}$  and  $2.10^{\circ}$  were applied for  $\mu=0.15$  and  $\mu=0.41$ , respectively. Negative values indicate a forward inclination of the rotor shaft relative to the body-fixed vertical axis, a configuration commonly adopted to counteract nose-up pitching tendencies in low-speed forward flight.

**Table 7.** Trim solutions of X2TD rotor at different advance ratios.

Advance ratio (μ)	Upper rotor			Lower rotor		
	$\Theta_0$	$\theta_{1s}$	$\theta_{1c}$	$\Theta_0$	$\theta_{1s}$	$\theta_{\rm 1c}$
0.15	9.45°	-3.65°	3.29°	9.39°	3.16°	3.29°

# 4. Results and Discussion

Upon validation of the computational setup, a parametric investigation was conducted to examine the influence of IRS on the aerodynamic and acoustic characteristics of a coaxial rotor system under low- and high-speed forward-flight conditions ( $\mu = 0.15$  and  $\mu = 0.41$ ). Three different IRS values were considered for each flight condition to systematically evaluate their impact on the resulting changes in thrust, unsteady rotor blade loading, wake flow, acoustic signal characteristics, and noise contributions from individual components, including the upper and lower rotors and fuselage. Moreover, by comparing the isolated rotor and full-configuration results, the influence of fuselage-rotor aerodynamic interaction on performance and noise propagation is elucidated.

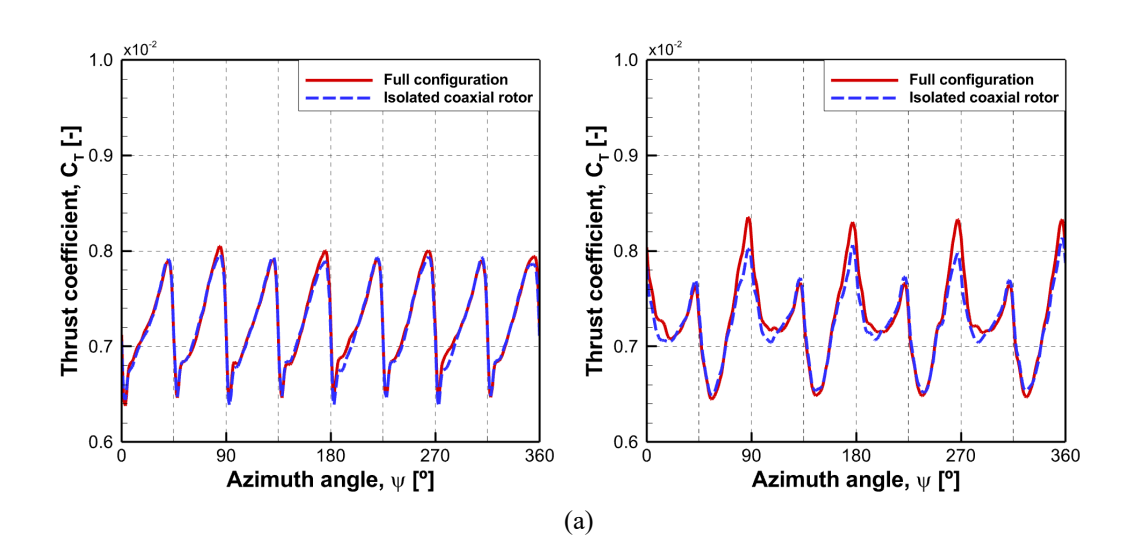
### 4.1 Effect of inter-rotor spacing Under Low-speed Forward-Flight Conditions

The influence of IRS on the aerodynamics of the coaxial rotor under low-speed forward-flight conditions was analyzed and compared for the isolated coaxial rotor and full-configuration models. Fig. 10 presents the effect of IRS on thrust in both models as a function of azimuth angle, and Table 8 presents the averaged thrust coefficient per revolution for each rotor. The upper and lower rotors generated vibrations at 45° intervals as the rotor blades passed one another, resulting in 8/rev vibrations. The difference in thrust in the isolated coaxial rotor and full-configuration models was predicted to be ~0.5% at the smallest IRS value. In terms of the lower rotor, a greater IRS value led to reduced interference from the wake generated by the upper rotor, creating additional thrust in both models. More interference occurred between the lower rotor and fuselage beneath the rotor in the full-configuration model than in the isolated coaxial rotor model. Compared to the isolated coaxial rotor model, the full-configuration model exhibited larger thrust fluctuation amplitude owing to a similar effect to ground interference between the wakes generated by the rotors and fuselage. Interference between the wakes generated by the upper and lower rotors decreased with increasing IRS value, reducing the thrust fluctuation amplitude for the lower rotor. The distance between the lower rotor and fuselage remained constant, and the

changes in interference between the lower rotor and fuselage were minimal as the upper rotor moved further away from the lower rotor (i.e., with increasing IRS value). Consequently, the thrust fluctuation amplitude in the isolated coaxial rotor model was lower than in the full-configuration model even with an increase in IRS value, and the averaged thrust was predicted to be 2% higher than the full-configuration model. The lower rotor generated a flow suction force around the lower surface of the upper rotor blade, leading to a decrease in thrust of the upper rotor and an increase in thrust fluctuation amplitude. This force weakened with increasing IRS value, enhancing the thrust of the upper rotor and reducing vibrations. These tendencies were observed in both models, where the differences in thrust fluctuation amplitude were minimal.

Table 8. Averaged thrust coefficient of coaxial rotor under low-speed forward-flight conditions.

IRS	Isol	ated coaxial r	otor	Full configuration		
IKS	Upper	Lower	Total	Upper	Lower	Total
0.055	0.00723	0.00725	0.01448	0.00727	0.00729	0.01460
0.083	0.00736	0.00754	0.01490	0.00752	0.00735	0.01487
0.110	0.00750	0.00767	0.01518	0.00763	0.00750	0.01513



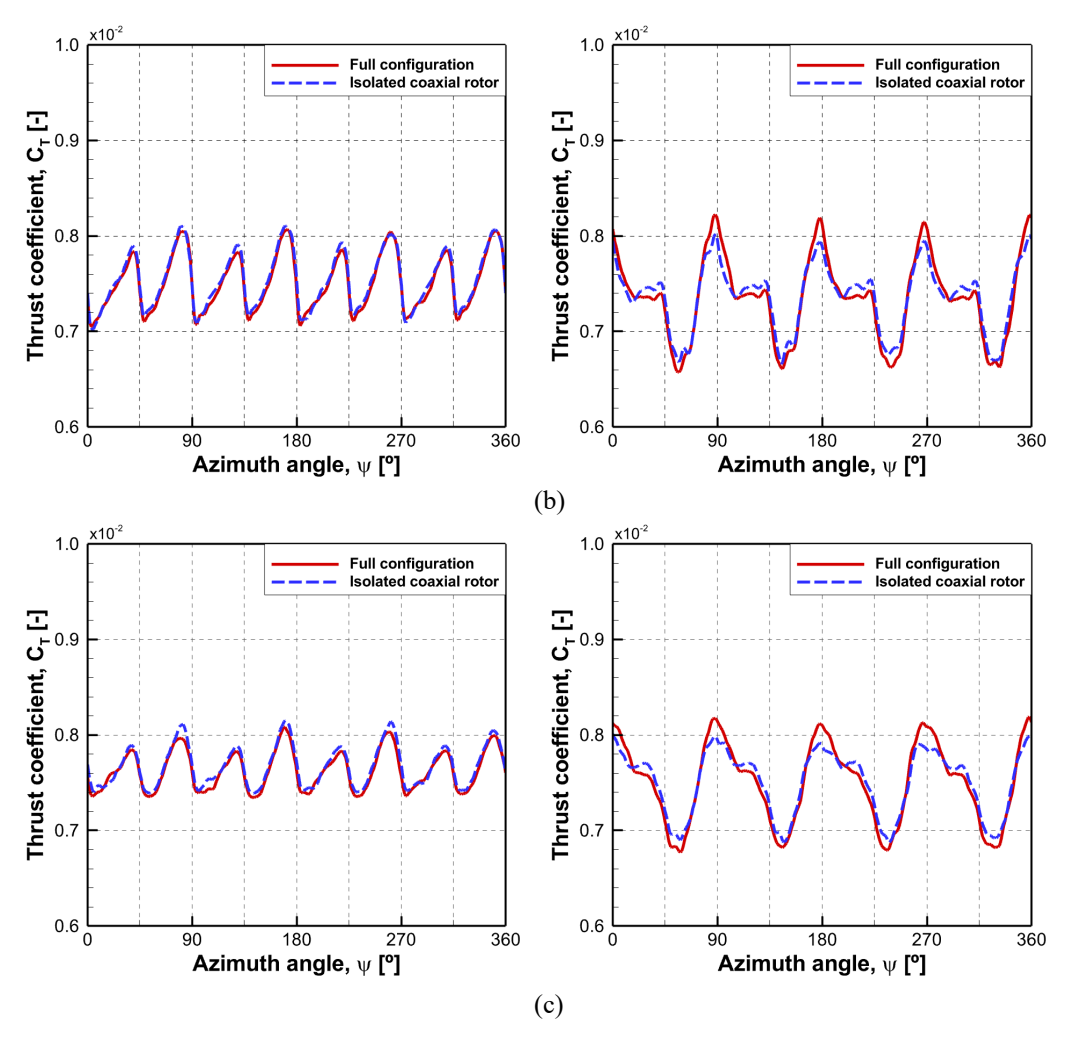
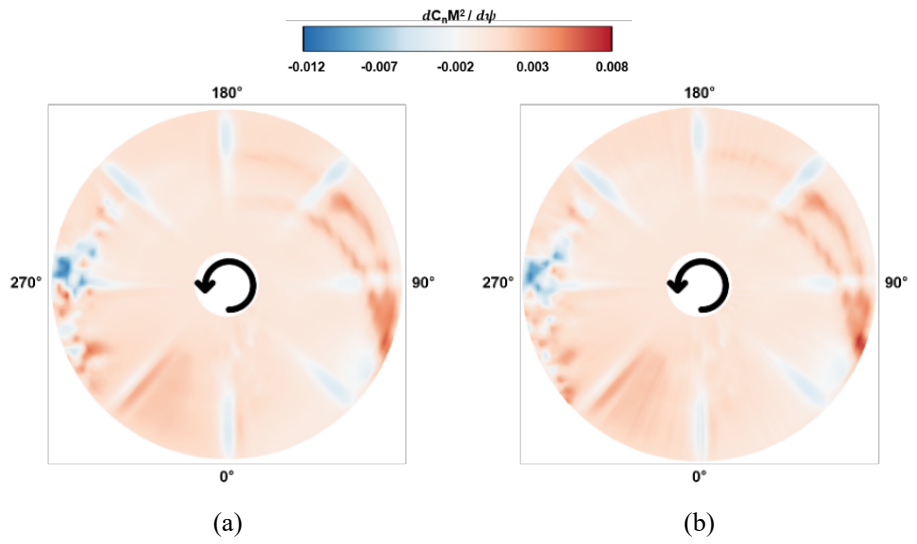


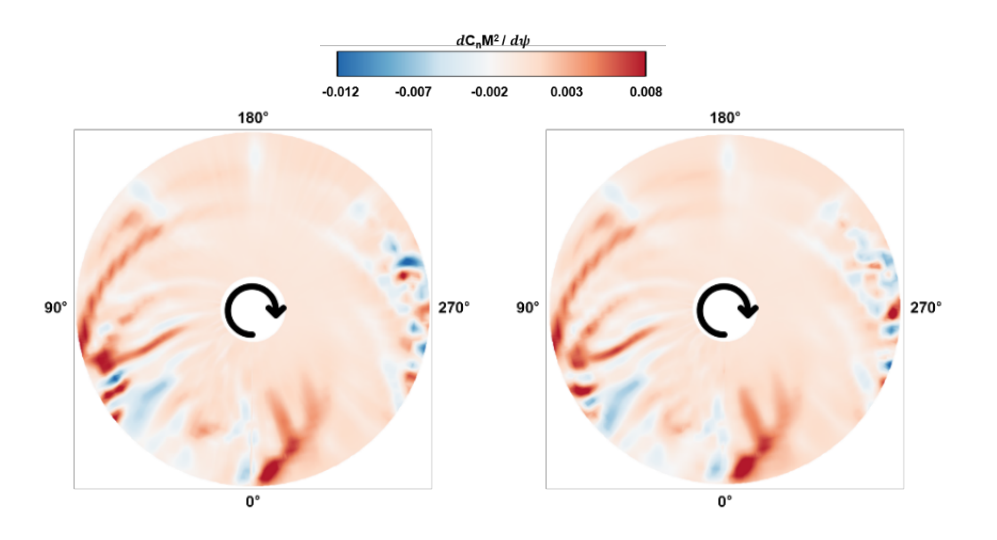
Fig. 10. Comparison of thrust coefficient ( $C_T$ ) as a function of azimuth angle ( $\psi$ ) under low-speed forward-flight conditions (left: upper rotor, right: lower rotor): (a) IRS = 0.055; (b) IRS = 0.083; (c) IRS = 0.110.

Figs. 11 and 12 present the variation and differences in normal force for the upper and lower rotor blades in the isolated coaxial rotor and full-configuration models under low-speed forward-flight conditions, illustrated as polar contour plots. The analysis was conducted for IRS = 0.083, where the mean thrust difference between the two rotors was the largest. For the upper and lower rotors, the normal force reached its maximum at an azimuth angle of 90°, corresponding to the advancing side, where the relative velocity of the blade was the highest. Conversely, the normal force was lower due to the reduced relative velocity at approximately 270°, corresponding to the retreating side. Interference occurred every 45° as the four-bladed upper and lower rotors passed one another, reducing the normal force at these locations. The lower rotor experienced more significant irregularities in normal force variation over a wider range due to interference from the wake generated by the upper rotor. Notably, the wake generated by the forward-flying upper rotor propagated downstream and interacted with the rear side of the lower rotor at an azimuth angle of 0°. This interaction led to a roll-up

phenomenon in the wake, increasing the pressure on the lower surface of the lower rotor blade and the normal force. As shown in Figs. 11 and 12, BVI differences between the full-configuration and isolated coaxial rotor models appeared at 270° for the upper rotor, corresponding to the retreating side, and at 90° and 270° for the lower rotor, corresponding to the advancing and retreating sides, respectively. Strong tip vortex generated at the lower rotor blade interacted with the fuselage, causing changes in unsteady loading. Consequently, the most significant load variations occurred at 90° and 270°, where the velocity differences between the upper and lower rotor blades were the greatest, leading to BVI differences between models. For the upper rotor blade, interference with the lower rotor blade was minimal at 90°, where the relative velocity was high. However, interaction with the lower rotor blade increased at 270°, where the relative velocity was lower, leading to a more pronounced BVI difference between models.



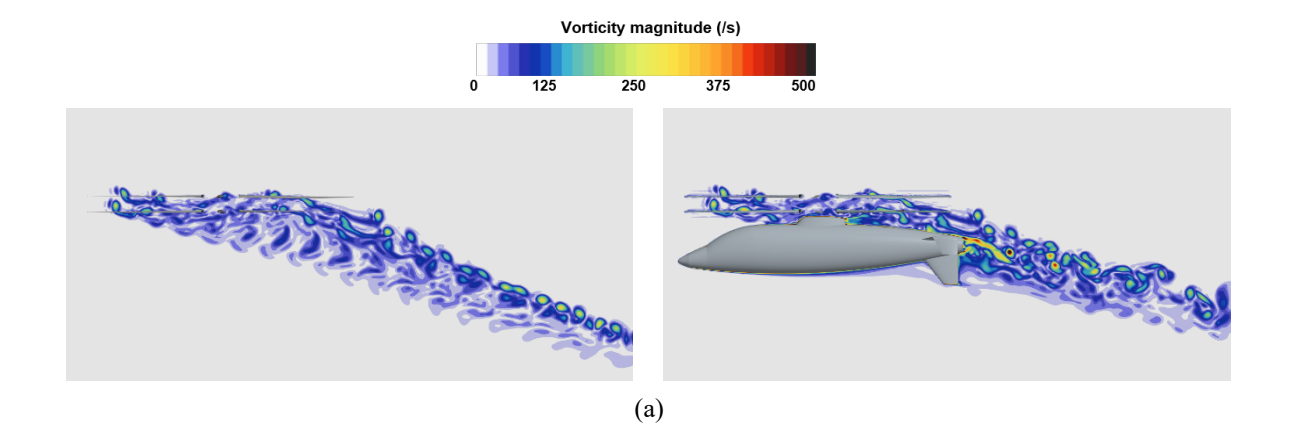
**Fig. 11.** Comparison of BVI polar contours of upper rotor blade at IRS = 0.083 under low-speed forward-flight conditions: (a) isolated coaxial rotor; (b) full configuration.



(a) (b)

**Fig. 12.** Comparison of BVI polar contours of lower rotor blade at IRS = 0.083 under low-speed forward-flight conditions: (a) isolated coaxial rotor; (b) full-configuration.

Fig. 13 shows the influence of IRS on the wake structures in the isolated coaxial rotor and full-configuration models using vorticity contour plots. In both models, an increase in the IRS value resulted in reduced interference between the wakes generated by the upper and lower rotors. For instance, when IRS = 0.055, the downwash produced by the wake from the upper rotor interfered with the lower rotor and merged with its wake, forming a complex super vortex structure that led to sustained strong vorticity as the wake propagated downstream. By contrast, at higher IRS values of 0.083 and 0.110, the downwash from the wake generated by the upper rotor induced less interference with the lower rotor and the merging point of the two wakes moved farther downstream. Notably, at IRS = 0.110, interference between the wakes generated by the upper and lower rotors was negligible except in the rear region corresponding to the azimuth angle of 0° of the lower rotor. The vortex formed by the wake of the upper rotor also remained more distinct, merging with the wake of the lower rotor on a smaller scale. When comparing the wake structures in the isolated coaxial rotor and full-configuration models at different IRS values, strong vorticity was observed around the fuselage due to its interaction with the wake generated by the lower rotor, which was in close proximity. The interference between the wakes of the upper and lower rotors decreased with increasing IRS. However, the wakes generated by the fuselage and lower rotor merged to form a super vortex, which rolled up and combined with the wake generated by the upper rotor to create an even larger vortex. These results highlighted that the full-configuration model exhibited distinct wake structures compared to the isolated coaxial rotor model, potentially exerting a greater influence on flow turbulence.



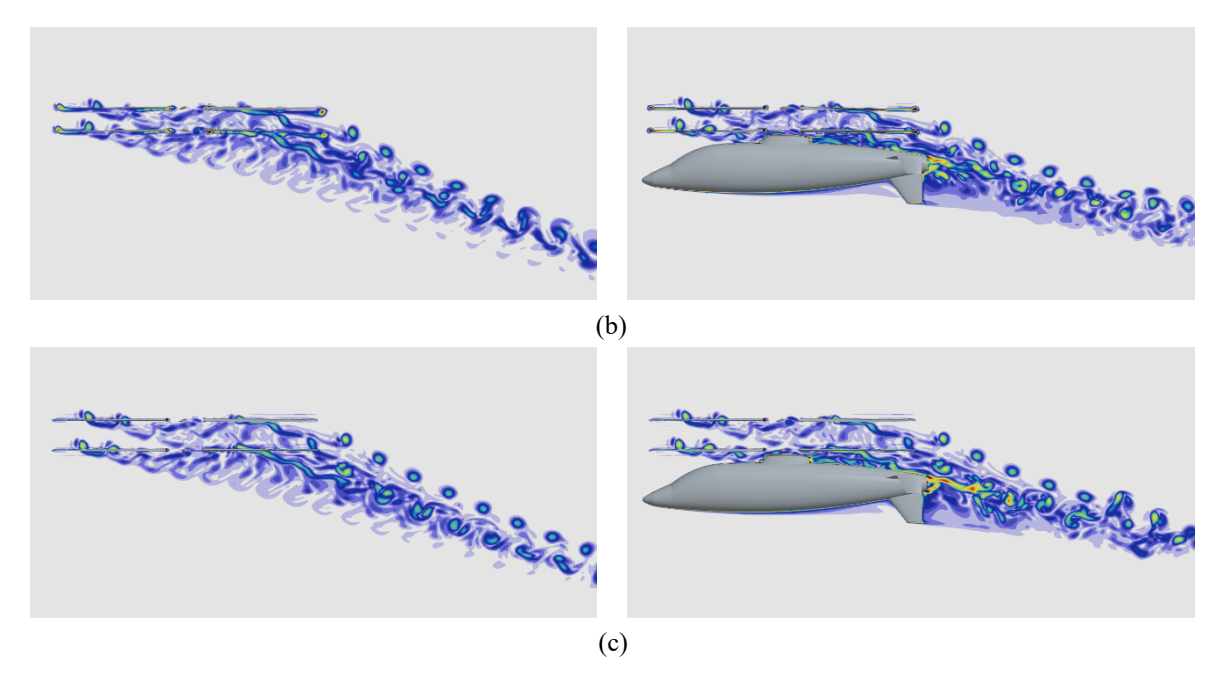


**Fig. 13.** Comparison of vorticity contours around coaxial rotor helicopter under low-speed forward-flight conditions (left: isolated coaxial rotor, right: full configuration): (a) IRS = 0.055; (b) IRS = 0.083; IRS = 0.110.

Unlike the isolated coaxial rotor, the full configuration, which includes the fuselage, can experience interference between the wake generated by the coaxial rotor and the fuselage. This interaction may induce a pitching moment on the fuselage, potentially affecting the controllability of the helicopter. Fig. 14 presents the effect of IRS variation on the pitching moment on the fuselage in the full-configuration model. Interaction between the wakes generated by the upper and lower rotors with the fuselage occurred four times per revolution, resulting in an 8/rev fluctuation trend in the pitching moment. The wake generated by the lower rotor strongly interacted with the wake generated by the upper rotor, producing a large and intense super vortex. Similarly, the wake generated by the upper rotor directly interfered with the fuselage. Consequently, the 1st, 3rd, 5th, and 7th fluctuations caused by interference with the lower rotor, as well as the 2nd, 4th, 6th, and 8th fluctuations caused by interference with the upper rotor, were most pronounced at IRS = 0.055. Interference between the wakes generated by the upper and lower rotors decreased with increasing IRS value, leading to a reduction in vorticity strength. Furthermore, the wake generated by the upper rotor propagated farther behind the fuselage, reducing the scale of interference with the fuselage and diminishing the thrust fluctuation amplitude. Consequently, the pitching moment decreased by 6.5% and 14.3% for IRS values of 0.083 and 0.110, respectively, enhancing the controllability of the coaxial rotor helicopter. The aerodynamic variations in the isolated coaxial rotor and fullconfiguration models under low-speed forward-flight conditions were analyzed and compared at different IRS

values. Unlike the isolated coaxial rotor model, the full-configuration model exhibited a larger thrust fluctuation amplitude and stronger vorticity near the fuselage due to interference between the wake generated by the coaxial rotor and fuselage. This interference induced a pitching moment on the fuselage as shown in Fig. 14.

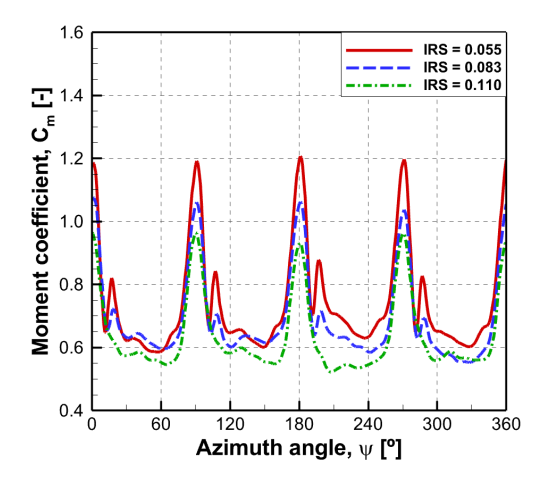


Fig. 14. Comparison of moment coefficient (C<sub>m</sub>) of fuselage as a function of azimuth angle (ψ) at different IRS values under low-speed forward-flight conditions.

Five microphones were positioned to predict the noise generated by the coaxial rotor helicopter. Table 9 presents their elevation angles. Each microphone was positioned at a distance of 10R from the center of the lower rotor, with elevation angles ranging from -180° to 0° at -45° intervals. Microphones 1 and 5, located at -180° and 0°, respectively, were most influenced by thickness noise. Microphones 2 and 4, positioned at -135° and -45°, respectively, were primarily affected by steady loading noise, including BVI noise caused by interference between the blades and wake vortices. Microphone 3, placed at -90°, was predominantly influenced by unsteady loading noise from wake interactions generated by the rotor blades.

Table 9. Locations of microphones as a function of elevation angle.

Table 7. Zerwiche et introprente de d'introde et et et et d'introde de die					
Microphone number	Elevation angle				
1	-180°				
2	-135°				
3	-90°				
4	-45°				
5	0°				

Fig. 15 shows the acoustic pressure variations at each microphone location as a function of azimuth angle in the isolated coaxial rotor and full-configuration models under low-speed forward-flight conditions at IRS = 0.110. The acoustic pressure fluctuated the least and the fluctuation amplitude was the smallest at microphones 1 and 5, where thickness noise was dominant and loading noise had a minimal effect. The overall trend in acoustic pressure variation was similar in both models at these microphone locations. Microphones 2 and 4, which were heavily influenced by steady loading noise, including BVI noise, exhibited a consistent 4/rev fluctuation pattern with similar amplitudes. Owing to the influence of loading noise, the acoustic pressure variations at microphones 2 and 4 exhibited more complex trends compared to microphones 1 and 5, with more frequent fluctuations. Unsteady loading noise was generated at microphone 3 due to interference between the wakes generated by the upper and lower rotors, as well as the flow suction force generated by the lower rotor. Consequently, the fluctuation amplitude of acoustic pressure was highest at microphone 3 and smaller-scale fluctuations frequently occurred within individual peaks. In the full-configuration model, unlike in the isolated coaxial rotor model, the wakes generated by both rotors interacted with the fuselage, creating additional interference. Consequently, the downward-propagating flow was reduced in the full-configuration model, leading to a predicted noise level that was 3 dB lower than in the isolated coaxial rotor model.

The results presented in Fig. 15 confirmed that the predicted acoustic pressure varied depending on the microphone location and presence of fuselage in the models. Given that the noise variation at each microphone location may also differ with IRS value under low-speed forward-flight conditions, the noise characteristics were analyzed as a function of IRS. Fig. 16 presents the noise analysis results in terms of overall sound pressure level (OASPL) for each microphone location, comparing the isolated coaxial rotor and full-configuration models at different IRS values. At microphones 1 and 5, the overall rotor size increased with increasing IRS value, leading to an increase in thickness noise. However, the overall noise variation remained small given that the influence of loading noise was minimal at these locations. Consequently, the noise level difference between IRS = 0.055 and IRS = 0.110 was predicted to be within 0.4 dB. At microphones 2 and 4, where steady loading noise was dominant, a greater IRS value reduced interference between vortices generated by the rotor blades and between the blades themselves. Consequently, the noise levels decreased by approximately 2–3 and 3–4 dB in the isolated coaxial rotor and full-configuration models, respectively. The BVI changes at the advancing and retreating sides of the upper and lower rotors in the full-configuration model were more significant than those in the isolated coaxial rotor model, leading to greater noise reduction in the full-configuration model. At

microphone 3, interference between the wakes generated by the upper and lower rotors decreased with increasing IRS value, reducing unsteady loading noise. Hence, the noise levels decreased by 4–8 and 5–10 dB in the isolated coaxial rotor and full-configuration models, respectively. These findings indicated that although both models exhibited similar noise reduction trends with increasing IRS value, the presence of fuselage caused an additional noise variation of approximately 1–2 dB in the full-configuration model.

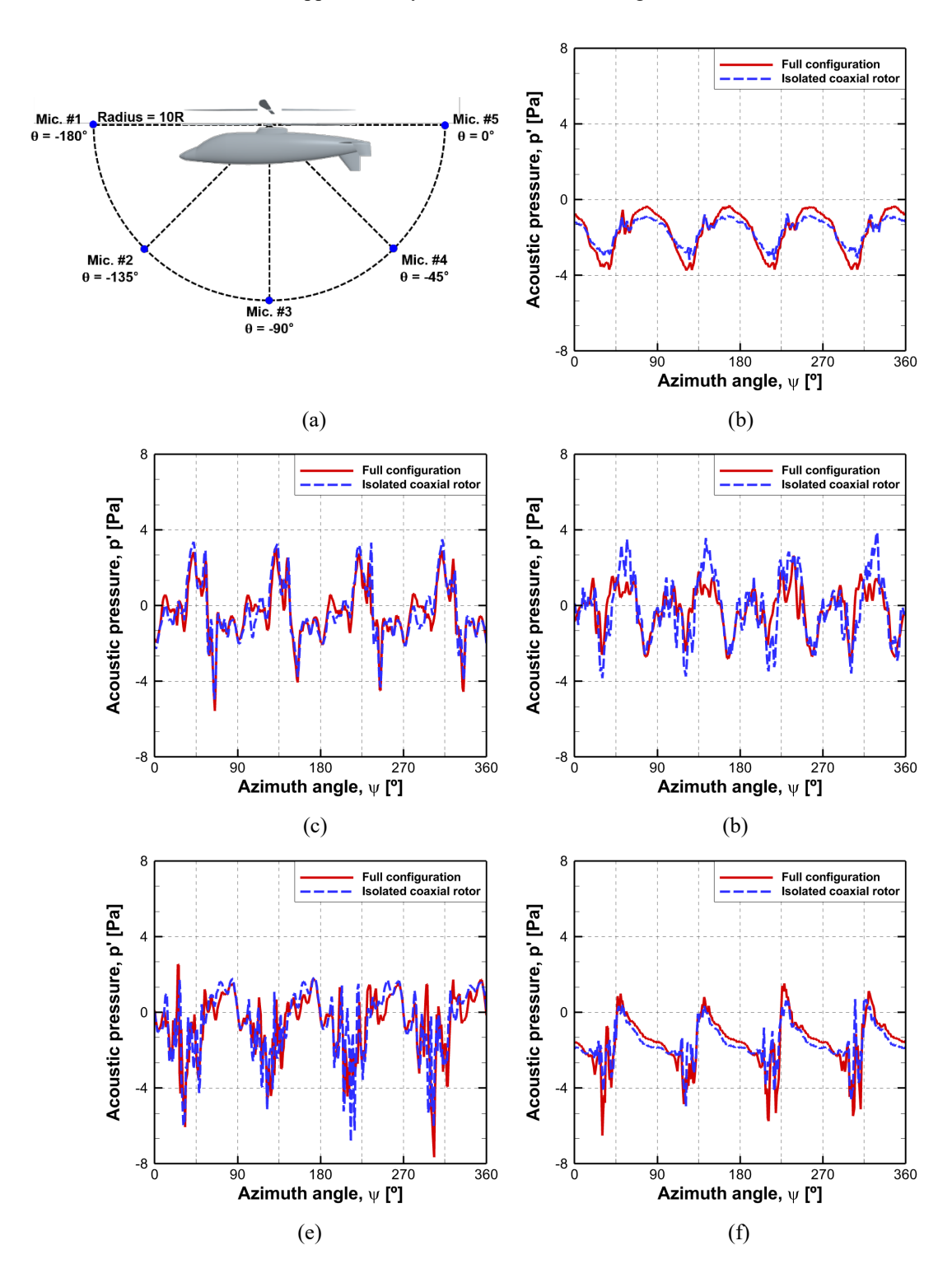
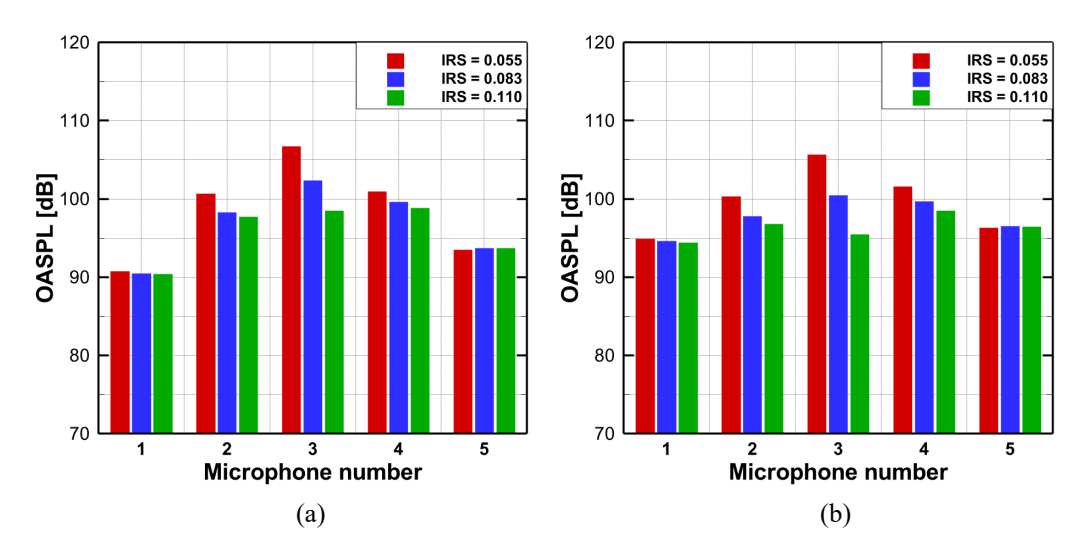


Fig. 15. Comparison of acoustic pressure as a function of azimuth angle ( $\psi$ ) at IRS = 0.110 under low-speed forward-flight conditions: (a) locations of microphones; (b) microphone 1,  $\theta = -180^{\circ}$ ; (c) microphone 2,  $\theta = -135^{\circ}$ ; (d) microphone 3,  $\theta = -90^{\circ}$ ; (e) microphone 4,  $\theta = -45^{\circ}$ ; (f) microphone 5,  $\theta = 0^{\circ}$ .



**Fig. 16.** Comparison of overall sound pressure level under low-speed forward-flight conditions: (a) isolated coaxial rotor; (b) full configuration.

Fig. 17 shows the noise contribution of each component under low-speed forward-flight conditions at IRS = 0.110 for the coaxial rotor. At microphone 1, the noise level generated by each rotor in the isolated coaxial rotor model was predicted to be approximately 3 dB lower than in the full-configuration model. In the full-configuration model, although the noise generated by the fuselage was small, the wakes generated by the upper and lower rotors reflected off the front of the fuselage, amplifying the noise. Consequently, the noise level generated in the full-configuration model was predicted to be 4 dB higher than in the isolated coaxial rotor model. At microphone 2, the flow suction force generated by the lower rotor weakened with increasing IRS value, resulting in reduced generation of noise by the upper rotor. However, interference between the wakes generated by the upper and lower rotors persisted, and the lower rotor remained the dominant noise source. Microphone 2, influenced primarily by steady loading noise, exhibited minimal changes in steady loading characteristics with increasing IRS value in both models, as observed in Figs. 9, 10, and 13. Additionally, the noise contribution of the fuselage was relatively low, with the noise level difference between models remaining within 0.4 dB. At microphone 3, where unsteady loading noise had the most significant impact, the noise contributions of the upper and lower rotors in the isolated coaxial rotor model were predicted to differ by only 0.1 dB, indicating similar noise levels for both rotors. In the full-configuration model, the noise levels generated

by the fuselage and upper rotor were predicted to differ by less than 0.2 dB. Moreover, interference between the wake generated by the lower rotor and the fuselage increased unsteady loading noise, resulting in a noise level increase of 1 dB in the full-configuration model compared to the isolated coaxial rotor model. Overall, noise generated by the upper and lower rotors reflected off the fuselage in the full-configuration model, leading to a noise level reduction of 3 dB compared to the isolated coaxial rotor.

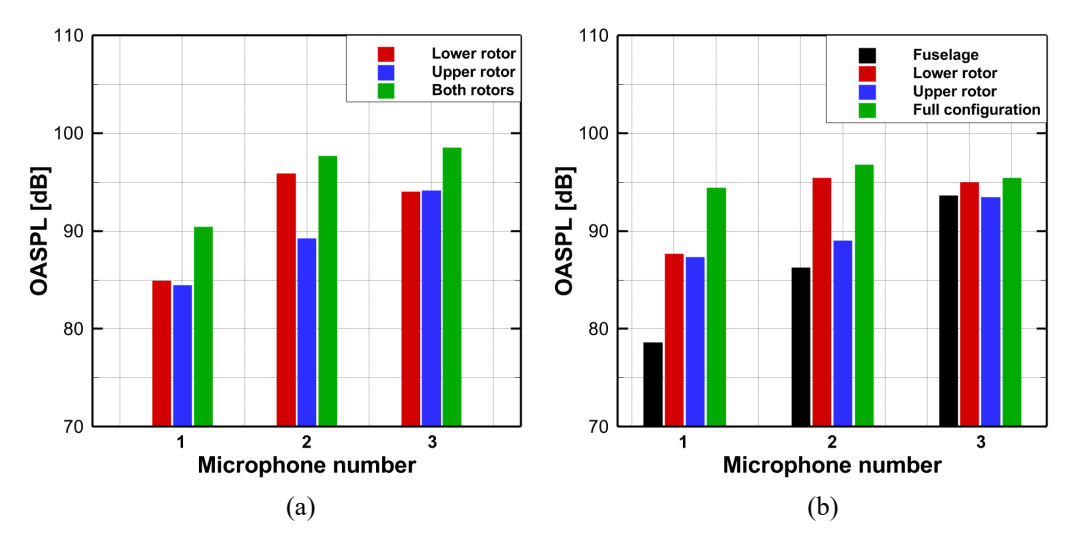
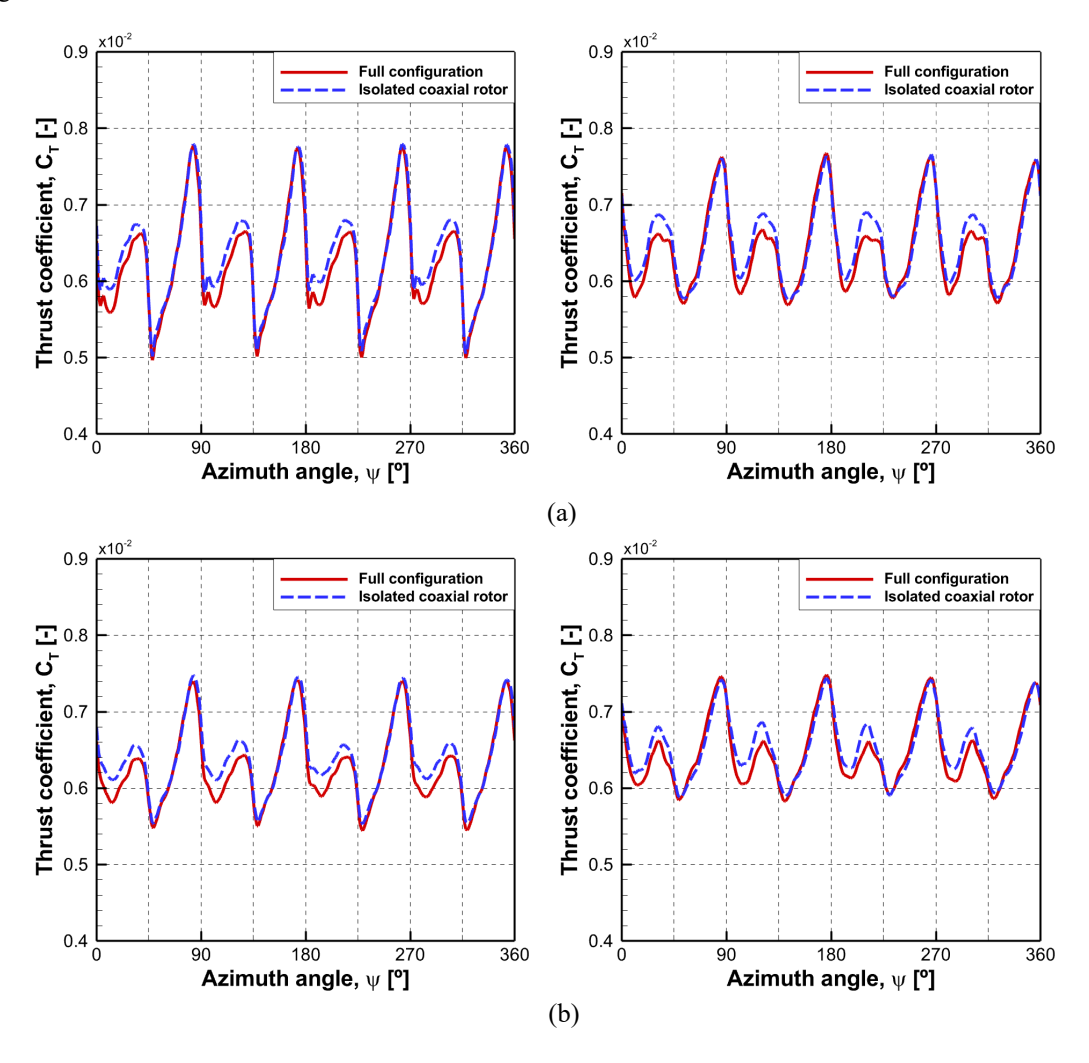


**Fig. 17.** Comparison of noise contribution at IRS = 0.110 under low-speed forward-flight conditions: (a) isolated coaxial rotor; (b) full configuration.

#### 4.2 Effect of Inter-Rotor Spacing Under High-speed Forward-Flight Conditions

The aerodynamic and acoustic variations with respect to IRS were analyzed in the isolated coaxial rotor and full-configuration models under low-speed forward-flight conditions. However, given that compound helicopters are designed for long-range and high-speed forward flight, the aerodynamic and acoustic variations at different IRS values were also investigated under high-speed forward-flight conditions. Fig. 18 compares the thrust variations in the both models under high-speed forward-flight conditions at different IRS values, while Table 10 presents the mean thrust coefficients per revolution for each rotor. At IRS = 0.055, where the spacing between the upper and lower rotors was the smallest, significant fluctuations in thrust were observed due to the flow suction force generated by the lower rotor and interference between the wakes generated by the upper and lower rotors. This condition resulted in the lowest predicted thrust. Interference between rotor blades diminished with increasing IRS value, with the highest thrust observed at IRS = 0.110. However, unlike under low-speed forward-flight conditions, the wakes generated by the upper and lower rotors rapidly propagated downstream under high-speed forward-flight conditions, reducing the scale of rotor-rotor interaction. Consequently, while

Table 10 indicates that the mean thrust at IRS = 0.110 was approximately 3.6% higher than that at IRS = 0.055 under low-speed forward-flight conditions, Table 8 indicates only a 0.7% increase in mean thrust under high-speed forward-flight conditions. Similar to under low-speed forward-flight conditions, interference between the wake generated by the lower rotor and the fuselage occurred in the full-configuration model under high-speed forward-flight conditions. This interference influenced the thrust of the upper rotor, given its occurrence near the lower surface of the upper rotor blades. The thrust in the full-configuration model was predicted to be approximately 1% lower than in the isolated coaxial rotor model. Notably, mutual interference between rotors decreased with increasing IRS value, leading to a similar thrust fluctuation in the isolated coaxial rotor and full-configuration at IRS = 0.110.



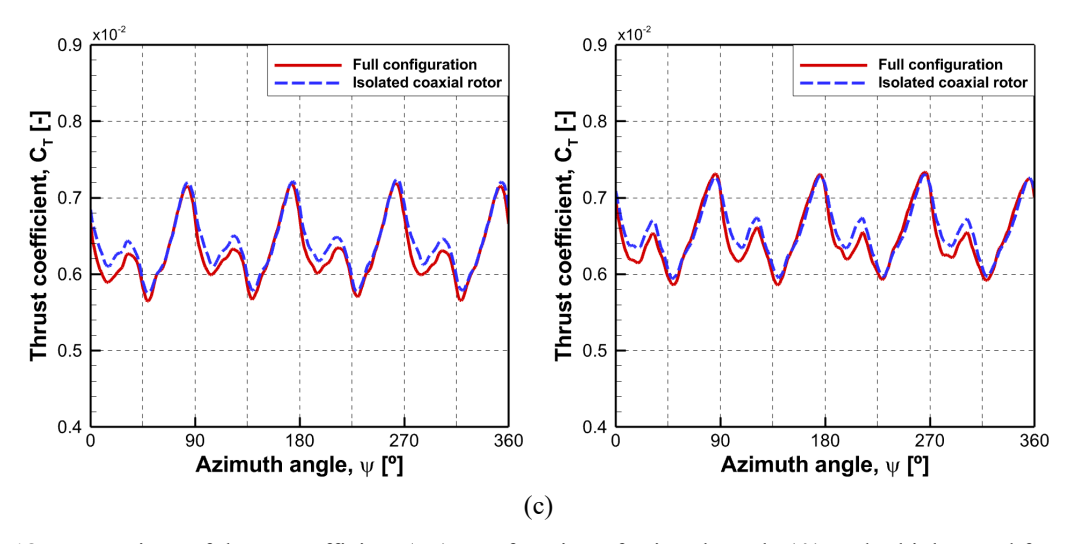


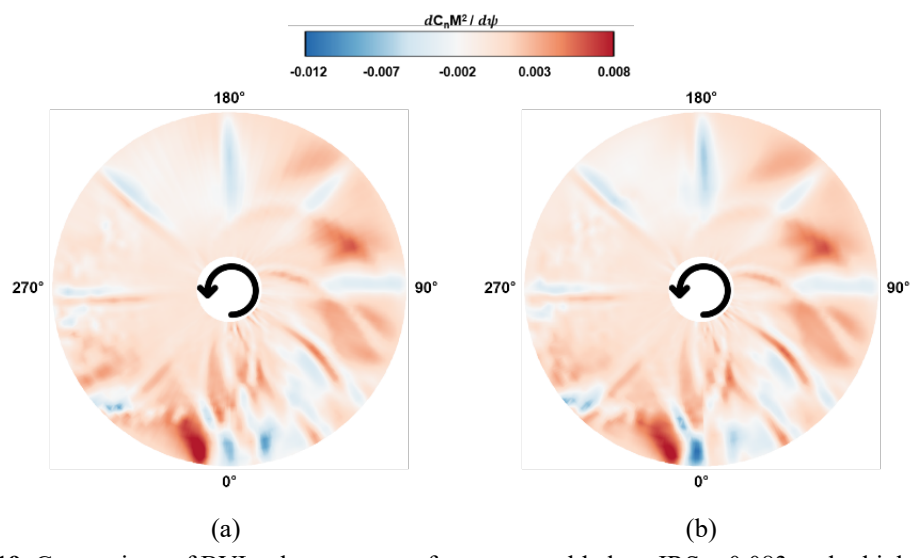
Fig. 18. Comparison of thrust coefficient ( $C_T$ ) as a function of azimuth angle ( $\psi$ ) under high-speed forward-flight conditions (left: upper rotor, right: lower rotor): (a) IRS = 0.055; (b) IRS = 0.083; (c) IRS = 0.110.

Table 10. Averaged thrust coefficient of coaxial rotor under high-speed forward-flight conditions.

IRS	Isol	Isolated coaxial rotor			Full configuration		
IKS	Upper	Lower	Total	Upper	Lower	Total	
0.055	0.00636	0.00651	0.01287	0.00625	0.00644	0.01269	
0.083	0.00639	0.00654	0.01293	0.00628	0.00648	0.01276	
0.110	0.00640	0.00656	0.01296	0.00629	0.00649	0.01278	

Figs. 19 and 20 illustrate the normal force distribution for the upper and lower rotor blades in the isolated coaxial rotor and full-configuration models under high-speed forward-flight conditions. The analysis is conducted for IRS = 0.083, with polar contour plots illustrating the normal force distribution as a function of azimuth angle. Similar to under low-speed forward-flight conditions, interference occurred every 45° when the upper and lower rotor blades passed one another, reducing the normal force in both models. However, under high-speed forward-flight conditions, the wakes generated by the upper and lower rotors propagated more backward than downward, increasing the frequency of BVI occurrence. Consequently, the magnitude and affected range of the normal force variations were more significant than those under low-speed forward-flight conditions. Notably, under low-speed forward-flight conditions, significant normal force variations were observed only on the lower rotor at an azimuth angle of 0°. By contrast, both rotors experienced normal force variations near this location under high-speed forward-flight conditions due to interference with their respective wakes. Additionally, at an azimuth angle of 270°, where the normal force was reduced due to the velocity

difference between rotors under low-speed forward-flight conditions, the reduction in normal force was less pronounced under high-speed forward-flight conditions. Comparing the differences in normal force variation between models, as shown in Figs. 19 and 20, the most significant BVI difference occurred at an azimuth angle of 0°. This was attributed to interaction between the wake generated by the lower rotor and the fuselage, which led to differences in BVI characteristics between models. Although the upper rotor exhibited more minor BVI differences than the lower rotor, interaction between the lower rotor and fuselage-induced complex flow patterns around the lower surface of the upper rotor blades, causing minor variations in BVI effects.



**Fig. 19.** Comparison of BVI polar contours of upper rotor blade at IRS = 0.083 under high-speed forward-flight conditions: (a) isolated coaxial rotor; (b) full configuration.

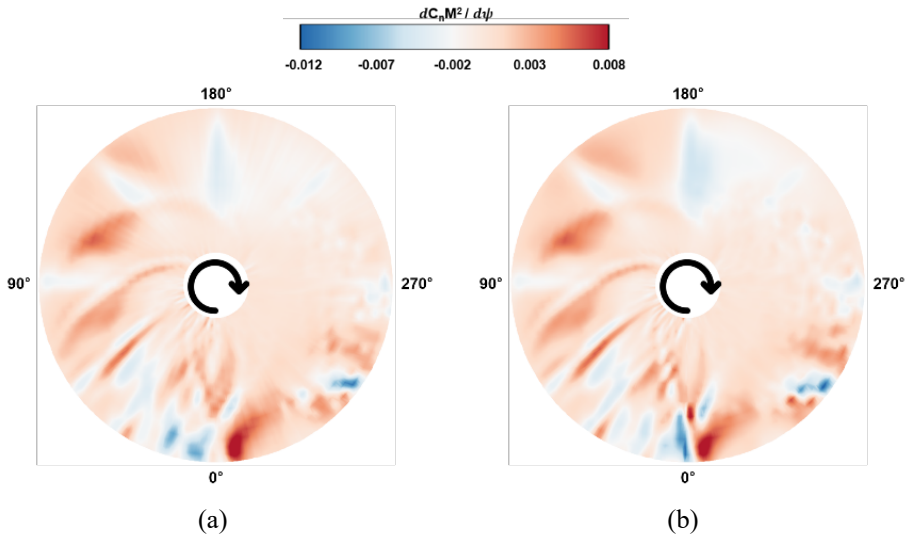


**Fig. 20.** Comparison of BVI polar contours of lower rotor blade at IRS = 0.083 under high-speed forward-flight conditions: (a) isolated coaxial rotor; (b) full configuration.

Under high-speed forward-flight conditions, the scale of interference between the wakes generated by the upper and lower rotors decreased, and the thrust variation generated by the rotors became negligible beyond a certain IRS value range. The impact of interference between the lower rotor and fuselage on the flow field was subsequently analyzed through observations of the wakes in the isolated coaxial rotor and full-configuration models. Fig. 21 illustrates the effect of IRS on the wakes generated in the isolated coaxial rotor and fullconfiguration models under high-speed forward-flight conditions, presented as vorticity contour plots. The wakes generated by the upper and lower rotors propagated backward under high-speed forward-flight conditions at all IRS values, causing interference with rotor blades and strong vorticity near the rotor hub. At IRS = 0.055, the close spacing between the upper and lower rotors caused their wakes to roll up, increasing interference with rotor blades and amplifying vorticity strength. Although the two wakes eventually merged, the flow propagated quickly, leading to rapid turbulence dissipation with minimal changes in vorticity strength. Interference between the wakes generated by the rotors and between the wakes and rotors themselves decreased during the initial stages of wake formation with increasing IRS value, resulting in weaker vorticity, and the merging point of the two wakes shifted farther downstream. At IRS = 0.110, no significant interference was observed beyond BVI for each rotor, and the upper and lower rotors operated independently without affecting one another. In the isolated coaxial rotor model, an increase in the IRS value reduced rotor-rotor interference, resulting in an overall decrease in vorticity around the flow field. By contrast, the full-configuration model exhibited stronger vorticity around the rotors compared to the isolated coaxial rotor model due to interference between the wake generated by the lower rotor and the fuselage. This interference led to the formation of a more complex wake structure. Although the isolated coaxial rotor model exhibited a tendency toward reduced vorticity in the downstream region with increasing IRS value, the full-configuration model maintained strong vorticity as the flow propagated downstream. This persistence of turbulence was caused by interaction between the wakes generated by the fuselage and lower rotor, preventing dissipation. These observations indicated that the full-configuration model produced complex wake structures and strong vorticity, which were not observed in the isolated coaxial rotor model but were expected to influence noise characteristics.

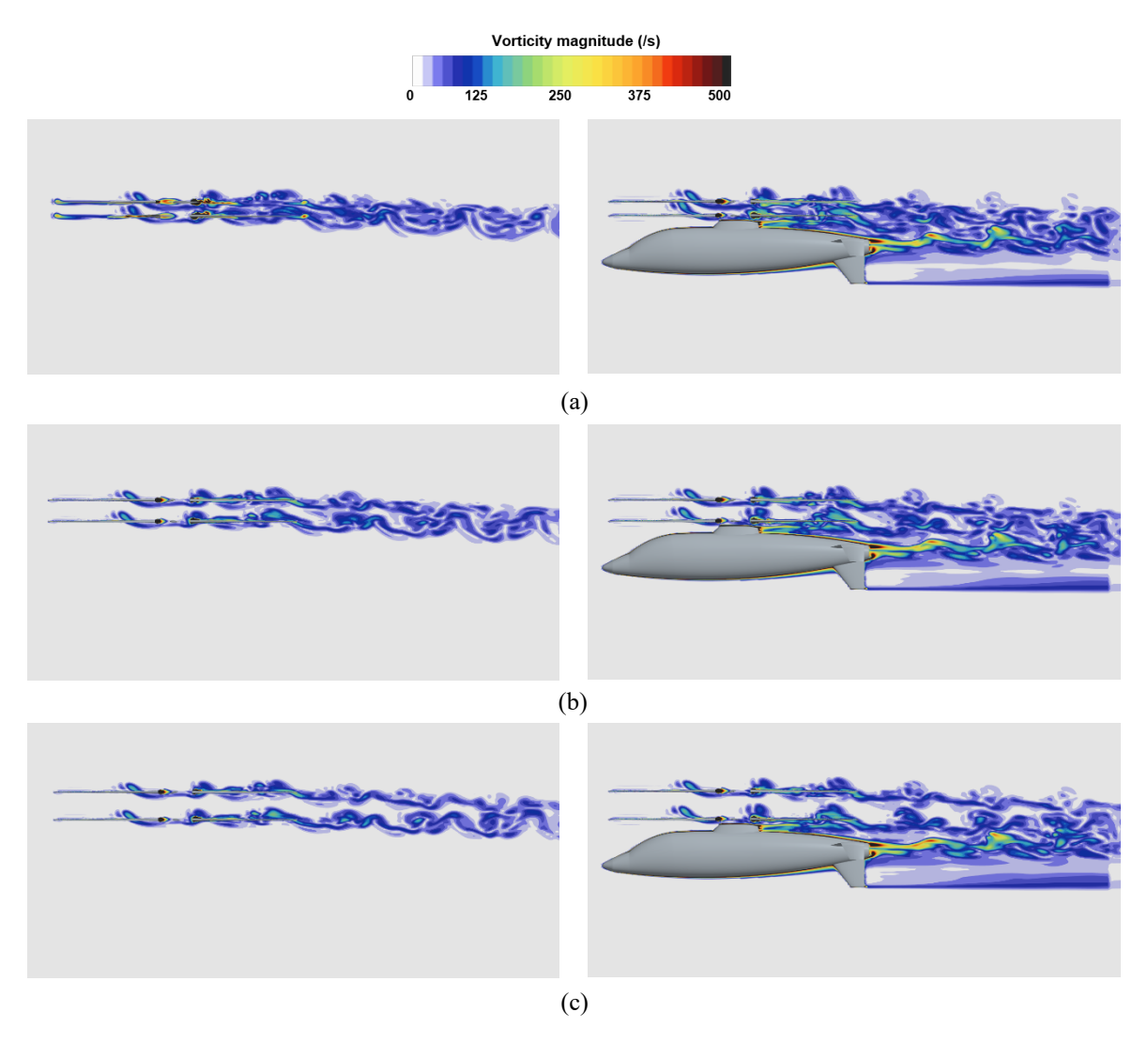


**Fig. 21.** Comparison of vorticity contours around coaxial rotor helicopter under high-speed forward-flight conditions (left: isolated coaxial rotor, right: full configuration): (a) IRS = 0.055; (b) IRS = 0.083; (c) IRS = 0.110.

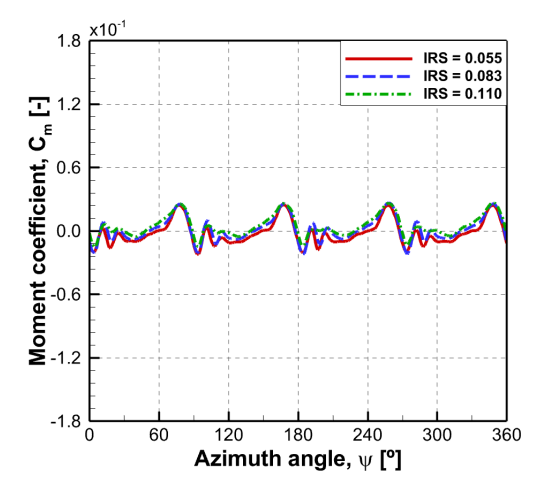


Fig. 22. Comparison of moment coefficient  $(C_m)$  of fuselage as a function of azimuth angle  $(\psi)$  at different IRS values under high-speed forward-flight conditions.

Fig. 22 presents the effect of IRS variations on the pitching moment on the fuselage under high speed forward-flight conditions. Similar to under low-speed forward-flight conditions, interference between the wakes generated by the upper and lower rotors and the fuselage resulted in eight pitching moment fluctuations per rotor revolution. The 2nd, 4th, 6th, and 8th fluctuations, influenced by the wake generated by the lower rotor, were less affected by interference with the wake generated by the upper rotor with increasing IRS value. However, given that the wakes rapidly propagated and the distance between the lower rotor and fuselage remained constant, the amplitude of these fluctuations did not significantly change. However, the 1st, 3rd, 5th, and 7th fluctuations, influenced by the wake generated by the upper rotor, exhibited a reduction in minor fluctuation amplitude with increasing IRS value due to decreased interference between the wake generated by the upper rotor and the fuselage. Although an increase in IRS value reduced interference between the upper rotor and fuselage under high-speed forward-flight conditions, the wake generated by the upper rotor propagated downstream before interacting with the fuselage. As a result, the pitching moment did not experience significant changes, and the mean pitching moment remained unaffected by IRS variations. These findings confirmed that IRS variations have little impact on the controllability of the coaxial rotor helicopter under high-speed forward-flight conditions.

When analyzing the aerodynamic variations in the isolated coaxial rotor and full-configuration models under high-speed forward-flight conditions at different IRS values, it was observed that the thrust growth rate was lower compared to that under low-speed forward-flight conditions. However, as we already discussed in Fig. 21, the sectional vorticity contours revealed interference differences near the fuselage between models, indicating the need to assess whether these differences influenced noise characteristics. Fig. 23 presents the acoustic pressure variations as a function of azimuth angle during one rotor revolution under high-speed forward-flight conditions at IRS = 0.110. The overall acoustic pressure trends at all microphone locations exhibited similarities to those observed under low-speed forward-flight conditions. At microphones 1 and 5, the full-configuration model exhibited more frequent but smaller fluctuations than the isolated coaxial rotor model under high-speed forward-flight conditions. Figs. 19 and 20 confirmed that BVI interference occurred more frequently under high-speed forward-flight conditions than under low-speed forward-flight conditions. Consequently, the fluctuation amplitude of acoustic pressure was greater at microphones 2 and 4, which were heavily influenced by steady loading noise, and more fluctuations were observed than under low-speed forward-flight conditions. At microphone 3, which was primarily affected by unsteady loading noise, the acoustic pressure amplitude in

the isolated coaxial rotor model was predicted to be larger than in the full-configuration model in the azimuth ranges of 45°-60°, 135°-150°, 225°-240°, and 315°-330°. This difference was attributed to part of the noise generated by the coaxial rotor propagating downward in the full-configuration model and being reflected by the fuselage. By contrast, the generated noise propagated directly to microphone 3 without interference in the isolated coaxial rotor model.

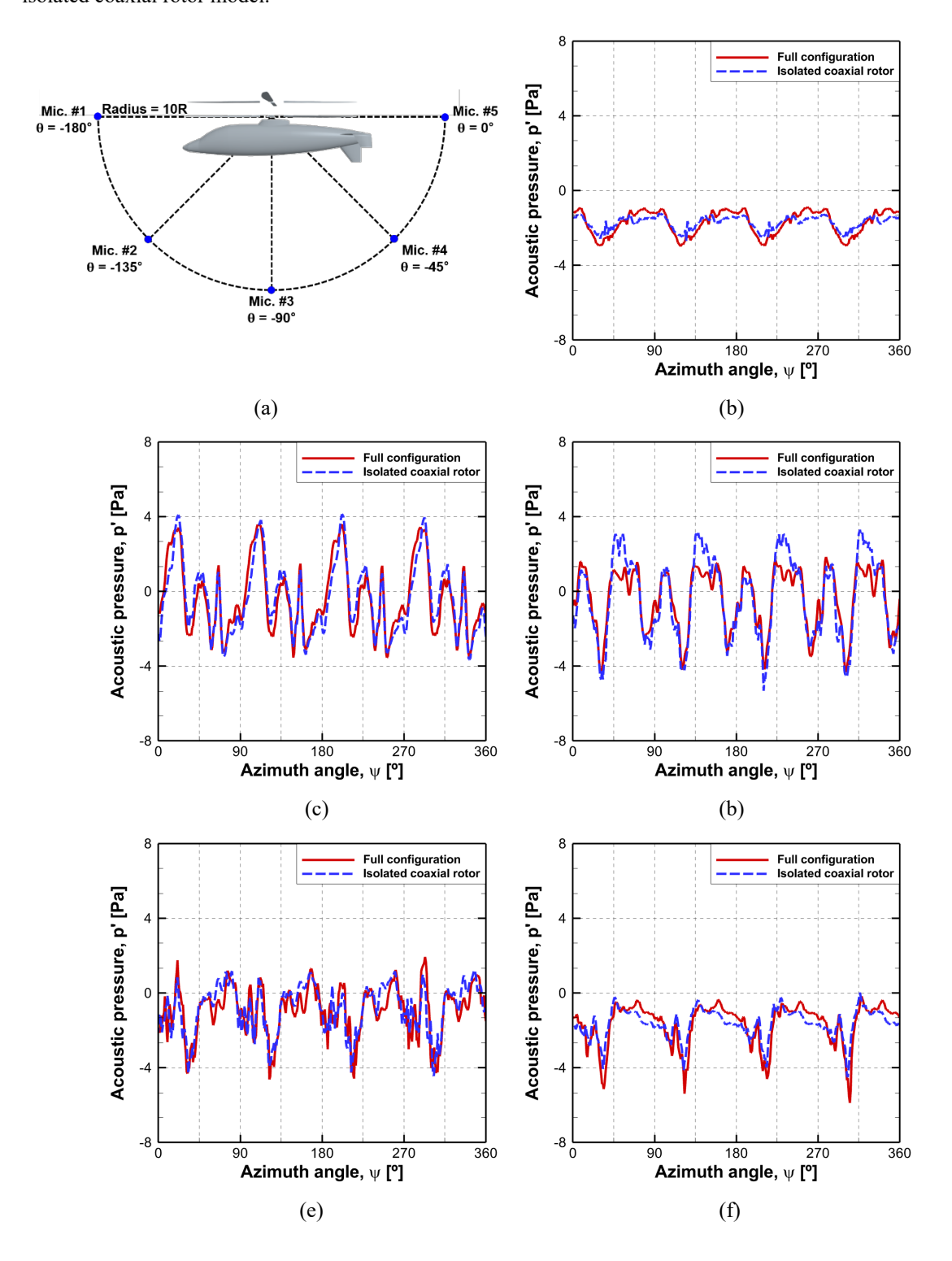
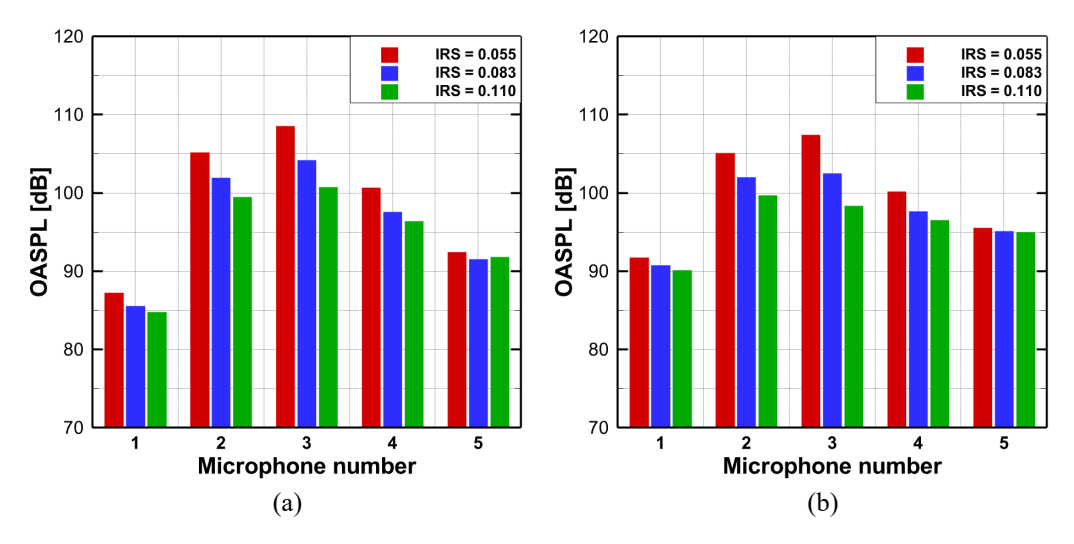
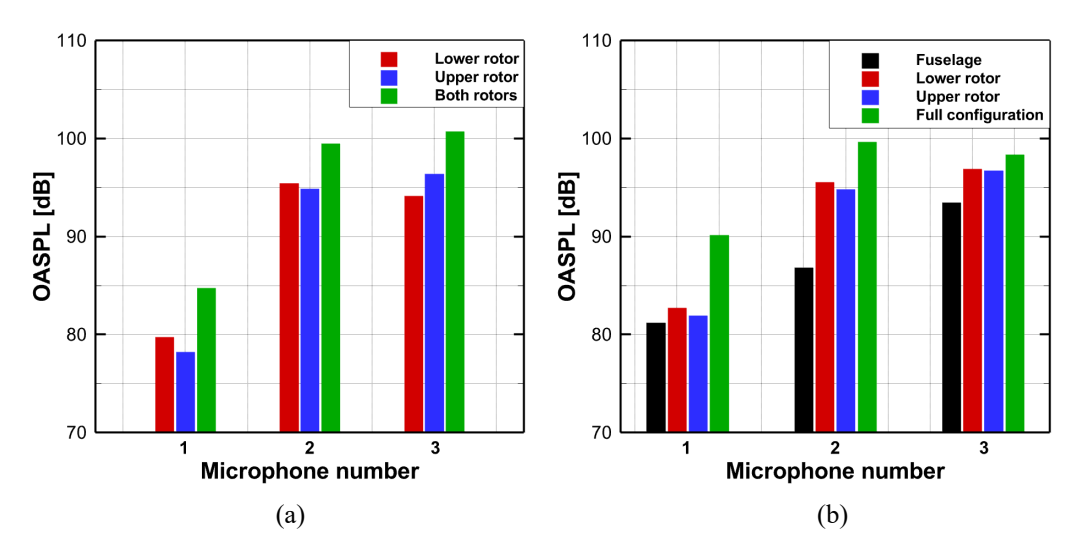


Fig. 23. Comparison of acoustic pressure as a function of azimuth angle ( $\psi$ ) at IRS = 0.110 under high-speed forward-flight conditions: (a) locations of microphones; (b) microphone 1,  $\theta = -180^{\circ}$ ; (c) microphone 2,  $\theta = -135^{\circ}$ ; (d) microphone 3,  $\theta = -90^{\circ}$ ; (e) microphone 4,  $\theta = -45^{\circ}$ ; (f) microphone 5,  $\theta = 0^{\circ}$ .

Fig. 24 presents the noise analysis results for each microphone in terms of OASPL under high-speed forward-flight conditions for both models at different IRS values. For microphones 1 and 5, where thickness noise was dominant, the noise levels decreased with increasing IRS value. In the full-configuration model, the noise levels were predicted to be approximately 5 and 2 dB higher than in the isolated coaxial rotor model at microphones 1 and 5, respectively, at the same IRS values. However, compared to microphones 2, 3, and 4, which were influenced by loading noise, the magnitude of noise reduction was relatively small. Under highspeed forward-flight conditions, the thrust variation remained within 1% with increasing IRS value. However, due to the larger BVI magnitude compared to low-speed forward-flight conditions, changes in steady loading noise with increasing IRS value were analyzed using microphones 2 and 4. The flow suction force of the lower rotor around the upper rotor and interference between the wakes generated by the upper and lower rotors decreased with increasing IRS value. Consequently, the noise levels under high-speed forward-flight conditions decreased by 3 and 5 dB at microphone 2 and by 3 and 4 dB at microphone 4 in the isolated coaxial rotor and full-configuration models, respectively, compared to low-speed forward-flight conditions. Figs. 22 and 23 demonstrated that the BVI differences between models were negligible, except near an azimuth angle of 0°, leading to a noise level difference of only 0.5 dB. The highest noise level was predicted at microphone 3 at IRS = 0.055. However, interference between the wakes generated by the upper and lower rotors and the fuselage decreased with increasing IRS value, reducing the noise level. Consequently, the noise levels in the isolated coaxial rotor and full-configuration models decreased by 4 and 8 dB with increasing IRS value, respectively. When comparing models, reflection by the fuselage of downward-propagating noise generated by the upper and lower rotors resulted in the noise levels consistently being 1-2 dB higher in the isolated coaxial rotor model than in the full-configuration model for all IRS values.



**Fig. 22.** Comparison of overall sound pressure level under high-speed forward-flight conditions: (a) Isolated coaxial rotor; (b) full configuration.



**Fig. 25.** Comparison of noise contribution at IRS = 0.110 under high-speed forward-flight conditions: (a) Isolated coaxial rotor; (b) full configuration.

Fig. 25 shows the noise contribution of each component in the coaxial rotor under high-speed forward-flight conditions at IRS = 0.110. Similar to under low-speed forward-flight conditions, the predicted noise level for each rotor in the isolated coaxial rotor model at microphone 1 was approximately 3 dB lower than that for the rotors in the full-configuration model. In the full-configuration model, the level of noise generated by the fuselage was predicted to be <1 dB lower than that generated by the rotors, indicating that the noise contribution of the fuselage was larger than under low-speed forward-flight conditions. Consequently, the level of total noise generated in the full-configuration model was predicted to be 5 dB higher than in the isolated coaxial rotor model. At microphone 2, interference between the upper and lower rotors decreased with increasing IRS value,

and the noise contributions from the two rotors were similar at IRS = 0.083 and IRS = 0.110. Additionally, the wake generated by the fuselage had minimal influence on rotor blade loading, resulting in negligible BVI differences between models. Consequently, the noise level difference between models for each rotor was within 0.4 dB, and the total noise level difference was predicted to be 0.2 dB. At microphone 3, the level of noise generated by the upper rotor was predicted to differ by only 0.4 dB between models, indicating similar noise levels. This was attributed to the near lack of interference with the upper rotor at the largest IRS value under high-speed forward-flight conditions, unlike at low IRS values under low- or high-speed forward-flight conditions, where the upper rotor experienced significant interference. Component-wise analysis revealed that the lower rotor in the full-configuration model exhibited a higher noise level by 3 dB compared to the isolated coaxial rotor model due to strong vortices generated by interference with the fuselage. Conversely, the noise contribution of the fuselage was reduced under high-speed forward-flight conditions compared to low-speed forward-flight conditions, as it was less affected by the wake generated by the upper rotor and predominantly influenced by interference with the lower rotor. When comparing total noise levels, reflection by the fuselage of the downward-propagating noise in the full-configuration model resulted in a 2 dB higher noise level than in the isolated coaxial rotor model.

## 5. Conclusions

This study investigated the aerodynamics and acoustics of forward-flight coaxial rotor helicopters via computational simulations conducted using isolated coaxial rotor and full-configuration models at different IRS values. The SA-IDDES numerical method was utilized to evaluate the aerodynamics of the coaxial rotor helicopter under low- and high-speed forward-flight conditions and the FW-H acoustic analogy method was employed to predict noise characteristics. For the coaxial rotor helicopter under low-speed forward-flight conditions, a greater IRS value resulted in a more significant reduction in rotor-rotor interaction compared to high-speed forward-flight conditions, leading to a mean thrust gain of approximately 3%. In the full-configuration model, the wake generated by the lower rotor interacted with the fuselage, generating a ground effect that caused more significant thrust amplitude fluctuations of the lower rotor. Under high-speed forward-flight conditions, the rotor wakes propagated more backward than low-speed forward-flight conditions, increasing the frequency of BVI occurrence. The noise level difference between the isolated coaxial rotor and

full-configuration models was predicted to be 0.2 dB owing to reduced interference from fuselage-generated vortices on the rotor blades. Under low- and high-speed forward-flight conditions, the noise levels decreased with increasing IRS value. However, greater noise reduction was observed at elevation angles of  $-45^{\circ}$ ,  $-90^{\circ}$ , and  $-135^{\circ}$ , which were more affected by steady and unsteady loading noise, compared to elevation angles of  $0^{\circ}$  and  $-180^{\circ}$ , where thickness noise was dominant. Under low- and high-speed forward-flight conditions, the most considerable noise difference between models was observed at an elevation angle of  $-90^{\circ}$ , which was highly influenced by unsteady loading noise. In the full-configuration model, the fuselage reflected noise propagating downward from the coaxial rotor, leading to a 2 dB lower noise level than in the isolated coaxial rotor model.

Although the present study shows that increasing IRS improves aerodynamic performance and reduces noise levels by mitigating rotor-rotor and rotor-fuselage interference, there are practical design constraints that limit the extent to which IRS can be increased. A larger IRS requires a bulkier hub system, which results in increased structural weight and drag. In particular, the hub is known to contribute up to half of the total drag in a coaxial rotor configuration, and the flow separation from this region can significantly influence both aerodynamic and acoustic behavior. Future studies will include hub and mast fairing geometries in the simulation model under various forward flight conditions. This will help to identify an optimal IRS range that achieves a balance between improved aerodynamic and acoustic performance and acceptable design penalties. In this study, the aerodynamic performance and acoustic characteristics of a coaxial rotor helicopter without a pusher thruster were investigated under different forward flight speeds and IRS conditions. However, modern coaxial rotor helicopters are designed as compound configurations equipped with a pusher thruster to enhance cruise performance. The interaction between the pusher thruster and the unsteady wake structures generated by the rotors and fuselage may significantly affect the aerodynamic loads and noise generation, especially under varying IRS and flight speed conditions. Therefore, future research will aim to analyze the aerodynamic and acoustic performance of coaxial compound helicopters with a pusher thruster to provide more comprehensive insight into the integrated system behavior.

## **Declaration of competing interest**

The authors declare that they have no competing financial interests or personal relationships that may have influenced the work reported in this study.

## Acknowledgments

This study was supported by Korea Research Institute for defense Technology planning and advancement (KRTI) grant funded by the Korea Government (Defense Acquisition Program Administration; DAPA) (KRIT-CT-23-010, VTOL Technology Research Center for Defense Applications 2025, Contribution: 80%). This work was supported by the Glocal University 30 Project Fund of Gyeongsang National University in 2025 (Contribution: 20%).

## References

- [1] K. Ferguson, D. Thomson, Performance comparison between a conventional helicopter and compound helicopter configurations, Proc. Inst. Mech. Eng. G J. Aerosp. Eng. 229 (13) (2015) 2441–2456.
- [2] X. Yin, H. Ma, W. Zhang, H. An, Z. Ke, L. Wang, B. Nie, Analysis of the controllability and stability of a hybrid high-speed compound helicopter with a new configuration, Int. J. Aeronaut. Space Sci. 25 (2024) 1205–1218.
- [3] A.M. Moodie, H. Yeo, Design of a cruise-efficient compound helicopter, J. Am. Helicopter Soc. 57 (3) (2012) 1–11.
- [4] C. Berrigan, M.J. Lopez, P. Ruckel, J.V.R. Prasad, Bell V-280 system identification: application of JIO methodology for hover model identification, Proc. Rotorcraft Handling Qualities Tech. Meeting (2020).
- [5] S. Zabunov, P. Getsov, G. Mardirossian, High-speed unmanned octo-rotor helicopters, Asian J. Nat. Appl. Sci. 3 (3) (2014).
- [6] C. Öhrle, F. Frey, J. Thiemeier, M. Keßler, Compound helicopter X3 in high-speed flight: correlation of simulation and flight test, J. Am. Helicopter Soc. 66 (1) (2021) 1–14.
- [7] M. Hirschberg, JMR technology demonstration update: the road to future vertical lift, Vertiflite 62 (1) (2014) 22–27.
- [8] R.V. Petrescu, 'Defiant', a today unique helicopter in the world, J. Aircraft Spacecraft Technol. 3 (2019) 92–106.
- [9] B.Y. Min, J. Kim, V. Klimchenko, J.C. Neiswonger, D. Griffiths, B.E. Wake, Full vehicle Helios model performance correlation with SB>1 Defiant® flight test, Proc. Vertical Flight Soc. 80th Annu. Forum Technol. Display (2024).
- [10] G. Jacobellis, G. Farhan, F. Matthew, Using control redundancy for power and vibration reduction on a coaxial rotor helicopter at high speeds, J. Am. Helicopter Soc. 64 (3) (2019) 1–15.

- [11] A. Bagai, Aerodynamic design of the X2 technology demonstrator main rotor blade, Proc. AHS Southwest Region Tech. Specialist's Meet. Next Generation Vertical Lift Technol. (2008).
- [12] P. Ventura Diaz, R. Caracuel Rubio, S. Yoon, High-fidelity computational analysis of ducted and coaxial rotors for urban air mobility, Proc. Vertical Flight Soc. 75th Annu. Forum Technol. Display (2019).
- [13] P. Pradeep, P. Wei, Energy-efficient arrival with RTA constraint for multirotor EVTOL in urban air mobility, J. Aerosp. Inf. Syst. 16 (7) (2019) 263–277.
- [14] P. Singh, P.P.F. Friedmann, Aeromechanics and aeroelastic stability of coaxial rotors, J. Aircraft 58 (6) (2021) 1386–1405.
- [15] H. Yeo, W. Johnson, Investigation of maximum blade loading capability of lift-offset rotors, J. Am. Helicopter Soc. 59 (1) (2014) 1–12.
- [16] H. Denton, M. Benedict, H. Kang, Design, development, and flight testing of a tube-launched coaxial-rotor based micro air vehicle, Int. J. Micro Air Veh. 14 (3) (2022) 1–14.
- [17] J.I. Go, D.H. Kim, J.S. Park, Performance and vibration analyses of lift-offset helicopters, Int. J. Aerosp. Eng. 2017 (2017) 1865751.
- [18] R. Feil, J. Rauleder, C.G. Cameron, J. Sirohi, Aeromechanics analysis of a high-advance-ratio lift-offset coaxial rotor system, J. Aircraft 56 (1) (2019) 166–178.
- [19] P.F. Lorber, T.A. Egolf, An unsteady helicopter rotor: fuselage interaction analysis, NASA-CR-4178, NASA (1988).
- [20] J.G. Leishman, S. Ananthan, An optimum coaxial rotor system for axial flight, J. Am. Helicopter Soc. 53 (4) (2008) 366–381.
- [21] M. Ramasamy, Hover performance measurements toward understanding aerodynamic interference in coaxial, tandem, and tilt rotors, J. Am. Helicopter Soc. 60 (3) (2015) 1–17.
- [22] T. Nagashima, K. Nakanishi, Optimum performance and wake geometry of co-axial rotor in hover, J. Jpn. Soc. Aeronaut. Space Sci. 26 (293) (1978) 325–333.
- [23] H. Qi, G. Xu, C. Lu, Y. Shi, A study of coaxial rotor aerodynamic interaction mechanism in hover with high-efficient trim model, Aerosp. Sci. Technol. 84 (2019) 1116–1130.
- [24] K. Shinohara, Optimum aerodynamic character of the coaxial counter rotating rotor system, Graduation Thesis, Koku Hisho Kogaku (Flight Engineering), Helicopter Engineering I, National Defense Academy of Japan (1977).

- [25] H.W. Kim, R.E. Brown, A comparison of coaxial and conventional rotor performance, J. Am. Helicopter Soc. 55 (1) (2010) 12004.
- [26] S.H. Park, O.J. Kwon, Numerical study about aerodynamic interaction for coaxial rotor blades, Int. J. Aeronaut. Space Sci. 22 (2021) 277–286.
- [27] K. Hayami, H. Sugawara, T. Yumino, Y. Tanabe, M. Kameda, CFD analysis on the performance of a coaxial rotor with lift offset at high advance ratios, Aerosp. Sci. Technol. 135 (2023) 108194.
- [28] Z. Jia, S. Lee, Aerodynamically induced noise of a lift-offset coaxial rotor with pitch attitude in high-speed forward flight, J. Sound Vib., 491 (2021) 115737.
- [29] Z. Jia, S. Lee, Impulsive loading noise of a lift-offset coaxial rotor in high-speed forward flight, AIAA J. 58 (2) (2020) 687-701.
- [30] V. Sedlacek, K. Yadav, M. Asper, J. Sirohi, Experimental investigation of coaxial co-rotating and counterrotating rotor acoustics in hover, Proc. Vertical Flight Soc. 80th Annu. Forum Technol. Display (2024).
- [31] H. Xu, W. Wang, X. Chen, Q. Zhao, Numerical analysis of aeroacoustic characteristics for coaxial counter rotating propellers considering the self-interference effect, Aerosp. Sci. Technol. 152 (2024) 109358.
- [32] H. Qi, L. Jiang, T. Pu, W. Zhu, Numerical investigation on aerodynamic noise of rigid coaxial rotor in forward flight with lift-offset, Int. J. Aeroacoust. 24 (1–2) (2024) 68–69.
- [33] P. Anusonti-Inthra, The effects of the fuselage on a coaxial rotorcraft performance, aerodynamics, and structural dynamics, Proc. AIAA Scietech 2019 Forum (2019) 1110.
- [34] H. W. Kim, A. R. Kenyon, R. E. Brown, K. Duraisamy, Interactional aerodynamics and acoustics of a hingeless coaxial helicopter with an auxiliary propeller in forward flight, Aeronaut. J. 113 (1140) (2009) 65-78.
- [35] J. Kim, J. Ko, S. Lee, Aeroacoustic analysis of coaxial rotor with rotor-fuselage interaction, in: INTER-NOISE and NOISE-CON Congress and Conference Proceedings, Inst. Noise Control Eng. 259 (4) (2019) 5157–5164.
- [36] N.M. Chaderjian, Advances in rotor performance and turbulent wake simulation using DES and adaptive mesh refinement, Proc. 7th Int. Conf. Comput. Fluid Dyn. (2012).
- [37] H.S. Park, D. Linton, B. Thornber, Towards Detached-Eddy Simulation of flow around rotorcraft using Immersed Boundary Method, AIAA J. 58 (11) (2020) 4893–4907.

- [38] P.R. Spalart, W.H. Jou, M. Strelets, S.R. Allmaras, Comments on the feasibility of LES for wings, and on a hybrid RANS/LES approach, Advances in DNS/LES: Proc. 1st AFOSR Int. Conf. DNS/LES, Greyden Press (1997) 137–147.
- [39] P.R. Spalart, S. Deck, M.L. Shur, K.D. Squires, M.K. Strelets, A. Travin, A new version of Detached-Eddy Simulation, resistant to ambiguous grid densities, Theor. Comput. Fluid Dyn. 20 (2006) 181–195.
- [40] M. Breuer, N. Jovičić, K. Mazaev, Comparison of DES, RANS, and LES for the separated flow around a flat plate at high incidence, Int. J. Numer. Meth. Fluids 41 (3) (2003) 357–388.
- [41] M.L. Shur, P.R. Spalart, M.K. Strelets, A.K. Travin, A hybrid RANS-LES approach with delayed-DES and wall-modelled capabilities, Int. J. Heat Fluid Flow 29 (6) (2008) 1638–1649.
- [42] K.S. Brentner, An efficient and robust method for predicting helicopter high-speed impulsive noise, J. Sound Vib. 203 (1) (1997) 87–100.
- [43] F. Williams, E. John, D.L. Hawkings, Sound generation by turbulence and surfaces in arbitrary motion, Philos. Trans. R. Soc. Lond. A Math. Phys. Eng. Sci. 264 (1151) (1969) 321–342.
- [44] H. Xu, W. Wang, X. Chen, Q. Zhao, Numerical analysis of rotor aeroacoustic characteristics during collective pitch aperiodic variation in hover, Aerosp. Sci. Technol. 124 (2022) 107012.
- [45] D. Lockard, A comparison of Ffowcs Williams-Hawkings solvers for airframe noise applications, Proc. 8th AIAA/CEAS Aeroacoustics Conf. Exhibit (2002).
- [46] R.D. Harrington, Full-scale-tunnel investigation of the static-thrust performance of a coaxial helicopter rotor, NACA-TN-2318 (1951).
- [47] N.L. Barbely, N.M. Komerath, Coaxial rotor flow phenomena in forward flight, Proc. 2016 Int. Powered Lift Conf. (IPLC)/SAE Aerosp. Syst. Technol. Conf. (2016).
- [48] B.J. Passe, A. Sridharan, J. Baeder, Computational investigation of coaxial rotor interactional aerodynamics in steady forward flight, Proc. 33rd AIAA Aerodyn. Conf. (2015).
- [49] D. Walsh, S. Weiner, K. Arifian, T. Lawrence, M. Wilson, R. Blackwell, Development testing of the Sikorsky X2 technology demonstrator, Proc. AHS 65th Annu. Forum (2009).
- [50] D. Linton, R. Widjaja, B. Thornber, Simulations of tandem and coaxial rotors using a CFD-coupled rotor model, Proc. 21st Australas. Fluid Mech. Conf. (2018).
- [51] J.G. Leishman, M. Syal, Figure of merit definition for coaxial rotors, J. Am. Helicopter Soc. 53 (3) (2008) 290–300.

- [52] Y.M. Kwon, J.S. Park, S.Y. Wie, H.J. Kang, D.H. Kim, Aeromechanics analyses of a modern lift-offset coaxial rotor in high-speed forward flight, Int. J. Aeronaut. Space Sci. 22 (2) (2021) 338–351.
- [53] S. Delprat, J.L. Thomas, J.M. Moschetta, Aeroacoustic modeling of helicopter transonic rotor noise, Aerosp. Sci. Technol. 122 (2022) 107302.
- [54] S. Lee, K. Sharma, K.S. Brentener, Aeroacoustic analysis of a lift-offset coaxial rotor using high-fidelity CFD/CSD loose coupling simulation, J. Am. Helicopter Soc. 65 (1) (2020) 1–15.
- [55] M. Biava, L. Vigevano, Simulation of a complete helicopter: a CFD approach to the study of interference effects, Aerosp. Sci. Technol. 19 (1) (2012) 37–49.
- [56] B. Wang, C. Cao, Q. Zhao, X. Yuan, Z. Zhu, Aeroacoustic characteristic analyses of coaxial rotors in hover and forward flight, Int. J. Aeronaut. Space Sci. 22 (6) (2021) 1278–1292.
- [57] T. Yoon, S. Lee, J. Kim, Mission performance analysis of a conceptual coaxial rotorcraft for urban air taxi applications, Aerosp. Sci. Technol. 80 (2018) 1–11.
- [58] H. Denton, M. Benedict, Investigation of coaxial rotor performance for a gun-launched micro air vehicle, Proc. Vertical Flight Soc. 79th Annu. Forum Technol. Display (2023).
- [59] M. Biava, L. Vigevano, CFD prediction of air flow past a full helicopter configuration, Aerosp. Sci. Technol. 19 (1) (2012) 3–18.
- [60] W.J. Baars, D. Ragni, Low-frequency intensity modulation of high-frequency rotor noise, AIAA J. 62 (9) (2024) 3374–3390.
- [61] J. Smith, A. Brown, Flow confinement effects on sUAS rotor noise, Aerosp. Sci. Technol. 134 (2023) 107123.
- [62] C.P. Coleman, A survey of the theoretical and experimental coaxial rotor aerodynamic research, NASA TP-3675 (1997).
- [63] S. Lee, M. Dassonville, Iterative blade element momentum theory for predicting coaxial rotor performance in hover, J. Am. Helicopter Soc. 65 (4) (2020) 1–12.
- [64] J. Ko, S. Lee, Numerical investigation of inter-rotor spacing effects on wake dynamics of coaxial rotors, J. Aircraft 58 (2) (2021) 363–373.
- [65] H.Y. Xu, Z.Y. Ye, Coaxial rotor helicopter in hover based on unstructured dynamic overset grids, J. Aircraft 47 (5) (2010) 1820–1824.
- [66] Y. Yuan, R. Chen, P. Li, Trim investigation for coaxial rigid rotor helicopters using an improved aerodynamic interference model, Aerosp. Sci. Technol. 85 (2019) 293–304.

- [67] Z. Jia, S. Lee, Impulsive loading noise of a lift-offset coaxial rotor in high-speed forward flight, AIAA J. 58 (2) (2020) 687–701.
- [68] B. Sengupta, E. Esmaeilifar, M.S. Araghizadeh, S. Kang, H. Lee, L.P. Raj, R.S. Myong, Rotor-fuselage-intake aerodynamics and icing using vortex and Eulerian–Lagrangian computational fluid dynamics methods, AIAA J. 63 (3) (2025) 1–22.
- [69] M.S. Araghizadeh, B. Sengupta, H. Lee, R.S. Myong, Aeroacoustic investigation of side-by-side urban air mobility aircraft in full configuration with ground effect, Phys. Fluids 36 (8) (2024) 087160.
- [70] D. Kim, H. Jeong, S. Lee, H. Seol, Simulation-based analysis of active noise control efficacy on propeller noise with unsteady blade motion, J. Mech. Sci. Technol. 39 (5) (2025) 2507–2518.